Finite-Amplitude Evolution of Instabilities Associated with the Coastal Upwelling Front

SCOTT M. DURSKI AND J. S. ALLEN

College of Oceanic and Atmospheric Sciences, Oregon State University, Corvallis, Oregon

(Manuscript received 19 November 2004, in final form 31 January 2005)

ABSTRACT

A primitive equation model is used to study the finite-amplitude evolution of instabilities associated with the coastal upwelling front. Simulations of increasing complexity are examined that represent idealizations of summer conditions off the Oregon coast, including cases with steady and with time-variable wind in a domain with alongshore-uniform bathymetry and with time-variable wind in a domain with realistic Oregon coast bathymetry. The numerical results indicate that the fastest-growing mode in this system has approximately an 8–10-km alongshore wavelength but that, once the disturbances grow to finite amplitude, the predominant alongfront scale increases rapidly because of nonlinear effects. Separation of the total kinetic energy into contributions from the alongshore average flow and perturbation about that average shows that the initial growth of the perturbation kinetic energy is due to potential energy conversion, but transfer of energy from the kinetic energy of the alongshore average flow becomes important once the disturbances reach large amplitude. The time-variable wind simulations again show initial growth of small-scale instabilities followed by evolution to larger scales. In this case, however, even after larger-scale disturbances have developed on the upwelling front, smaller-scale patterns amplify along the front in response to each upwelling-favorable wind event. Realistic coastal bathymetry introduces additional alongshore topographic scales into the problem, but the formation of instabilities on small scales and evolution to larger scales are still ubiquitous. Where instabilities encounter strong curvature in the upwelling front produced by bathymetric effects, the upwelling front becomes highly contorted and horizontal variability is significantly enhanced.

1. Introduction

Upwelling is a frequent summertime occurrence off the Oregon coast. Southward-directed winds produce offshore transport in the oceanic surface layer, causing horizontal flow divergence near the coast that draws the pycnocline upward to the surface. Under sustained winds, the pycnocline breaches the surface as an upwelling front marked by warm surface waters offshore and colder, typically more nutrient rich, waters near the coast. Though generally parallel to the coastline, this front and the associated alongshore jet meander at a variety of scales as can commonly be observed in Advanced Very High Resolution Radiometer (AVHRR) satellite images of the sea surface temperature (Fig. 1). These across-shore deflections become of interest particularly when they reach large amplitude, because they can produce eddies, squirts, and filaments that transport significant amounts of heat, nutrients, and other biogeochemically important substances off the shelf. The variety of factors that determine the scales of these meanders include flow instability processes, bathymetry, coastline curvature, and spatial variation in the wind field. The effects of the last three of these are typically explored using primitive equation numerical ocean models, largely because of the fact that realistic variations in any make the fluid motion nonlinear and the equations intractable to analytical analysis or linearized approximations. In contrast, much research has been undertaken into the scales of upwelling frontal variability that flow instabilities introduce through the analysis of equations linearized about a steady equilibrium background state (Barth 1989a,b, 1994; McCreary et al. 1991; Fukamachi et al. 1995; Shi and Roed 1999; Eldevik and Dysthe 2002). Linear stability analysis has been exploited fruitfully to determine the potential properties of instabilities on the upwelling front in the coastal transition zone off Oregon and California (McCreary et al. 1991; Barth 1994; Fukamachi et al. 1995) and along the Iberian Peninsula (Shi and Roed 1999). Such studies focus on determining which scales of disturbance will grow fastest and what energetic exchange

Corresponding author address: Scott M. Durski, COAS, Oregon State University, Corvallis, OR 97331.
E-mail: sdurski@coas.oregonstate.edu

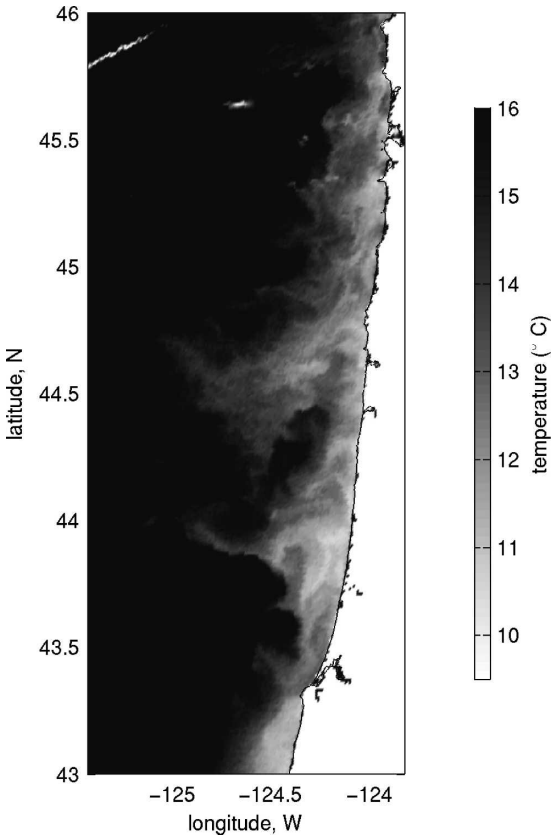

FIG. 1. An AVHRR satellite-derived image of sea surface temperature for the Oregon coastal region on 24 Aug 2003.

mechanisms are responsible for them. Studies utilizing different models (1.5 layer, 2 layer, primitive equation) and different background states yield somewhat differing results. In the layered models exploited by McCreary et al. (1991), Fukamachi et al. (1995), and Shi and Roed (1999), two scales of instabilities were found to exist: a longer mode with maximum growth rate generally between 50 and 100 km, which was associated with a mixed barotropic–baroclinic energy transfer process, and a shorter, faster-growing ageostrophic baroclinic mode, which asymptotically approached a maximum growth rate at zero wavelength (in the absence of mixing). The continuously stratified analog to this setup, which Fukamachi et al. (1995) also explored, had a maximum growth rate for the shorter instability at a wavelength of approximately 6 km. The modes in these studies differed from similar scale-separated modes found by Barth (1994) through linear analysis of a continously stratified primitive equation model. The longer-scale mode (70 km) in Barth's (1994) analysis was attributed to "classical" baroclinic instability as explained by Eady (1949) and Charney (1947). The shorter-scale mode, with maximum growth rate at approximately 17 km, while still associated with baroclinic energy transfer, had a significantly faster phase speed and different vertical structure from that found by Fukamachi et al. (1995). Differences in the specification of the background states in these studies presumably result in the different characteristics of the unstable modes. Still, in all cases the fastest-growing mode is the shorter-wavelength one. This shorter-wavelength disturbance is surface trapped in all cases and is loosely referred to as the "frontal mode." Such shallow, shorter-wavelength modes have been found in atmospheric studies of fronts as well. Yamazaki and Peltier (2001) found a deep synoptic-scale baroclinic mode and a shallow subsynoptic-scale instability in a linear analysis of a continuously stratified model of an atmospheric front.

While a number of the aforementioned studies utilized fully nonlinear numerical models to corroborate the results of their linear stability analysis, only a few have examined the finite-amplitude evolution of the disturbances. Those studies have indicated that the predominant scale of disturbance along the front increases over time. McCreary et al. (1991) suggested that the instabilities that developed in his system merged through wave–wave interactions into larger-scale features on a time scale of approximately 20 days. Shi and Roed (1999) found qualitatively similar results in their layered model numerical experiments based on the background flow of Fukamachi et al. (1995). Eldevik and Dysthe (2002) also explored the finite-amplitude evolution of the frontal instabilities on the Fukamachi background state in a study of spiral-eddy formation, but eliminated the possibility of "upscaling" by limiting their domain size to the length of the fastest growing mode. Yamazaki and Peltier (2001) described the increase in scale of the subsynoptic baroclinic instabilities that they observed in their atmospheric model as potentially associated with an eddy-draining mechanism (Klaassen and Peltier 1989). Alternately, Barth (1994) attributes the appearance of larger scales in his primitive equation numerical model of the instabilities associated with the California Coastal current, not to nonlinear interaction of disturbances, but rather to the slow growth of the longer-wavelength deep baroclinic mode.

The collection of information that these idealized studies provide attest to the great complexity these instability mechanisms will introduce into the real coastal ocean in which the bathymetry varies in space and the forcing varies temporally so that the "background state" is time dependent and spatially variable. A wind-forced upwelling system, such as is found off the coast of Oregon, evolves on a time scale comparable to the time scale of growth of the frontal instabilities associ-

ated with it. This makes definition of an appropriate steady background state for linear stability analyses or for use as initial conditions in a finite-amplitude numerical experiment problematic.

In this study we examine the development of frontal instabilities in the typical coastal situation of wind-forced time-varying background flows. A primitive equation numerical model with relatively high resolution and very weakly dissipative numerics generates energetic frontal meanders that bear strong qualitative resemblance to those observed through satellite imagery of the Oregon shelf. The model is utilized to explore the finite-amplitude evolution of the upwelling frontal instabilities in a series of idealized experiments that allow the extraction of useful quantitative and qualitative information about their nature. To understand the evolution of instabilities in the simplest evolving upwelling system, the fluid dynamical response in a channel with alongshore-uniform bathymetry and steady wind forcing is studied in detail first. This setting allows separation of the flow variables into an alongshore mean and perturbation about that mean for diagnosis of the interactions of the perturbations with the alongshore-mean flow. Two further simulations are examined in addition to the steady-wind, alongshore-uniform channel. Forcing by time-dependent observed winds off Oregon is considered in the same channel configuration to enable an assessment of the behavior of the instabilities when the alongshore-mean field has additional time variability consistent with that forced by realistic fluctuating winds. Last, time-dependent observed wind forcing is utilized in a domain with realistic Oregon coast bathymetry to examine the consequences on the instability process of time-variable forcing combined with alongshore spatial variability induced by the topography.

2. Model setup

The numerical model used in this study is the Regional Ocean Modeling System (ROMS) (Shchepetkin and McWilliams 2005). It is a primitive equation model formulated in finite-difference form with a sigma-coordinate representation in the vertical. For this study, potential density is the only prognostic scalar variable calculated. The advection scheme utilized is the third-order upwind scheme of Shchepetkin and McWilliams (1998). Mixing in the horizontal is Laplacian with small values of 2 $m^2 s^{-1}$ for both viscosity and diffusivity. The Mellor–Yamada level-2.5 closure scheme (Mellor and Yamada 1982) is used for vertical mixing. [Sensitivity to usage of the Large et al. (1994) *K*-profile parameterization was also tested and was found to give similar results.] Bottom stress is specified using a neutral quadratic bottom drag law, with a bottom roughness specified as 1 cm. Two different model domains are considered. Both are north–south periodic channels with a coastal wall along the eastern edge. A Cartesian coordinate system is used with *y* aligned north–south (positive northward), *x* aligned east–west (positive toward the coast), and *z* aligned vertically (Fig. 2). The western boundary is specified as a radiating open boundary. Tests were performed with a vertical wall condition at the offshore boundary that confirmed that the boundary conditions did not affect the solution behavior in the region of interest. An alongshore-uniform, smoothed representation of the typical across-shore depth profile off the Oregon coast is used in the first part of the study (Fig. 3). A dataset for the Oregon coast bathymetry between 43.25° and 45.6°N is used as the basis for the bottom topography in the latter part of the study. The data bathymetry is distorted slightly in the alongshore direction to produce a straight coastline and alleviate any need for masking or curvilinear horizontal coordinates. This data bathymetry is smoothed into a uniform alongshore section at both north and south ends of the domain to ensure continuity across the periodic boundaries (Fig. 2).

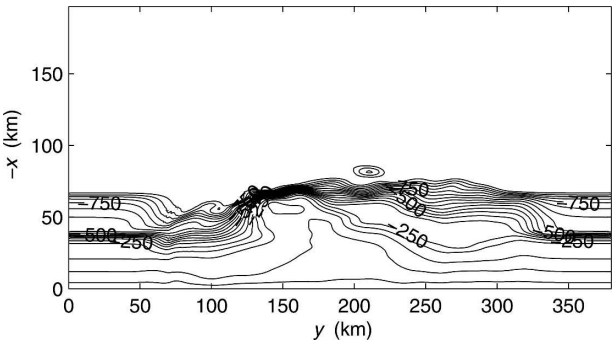

FIG. 2. Realistic bathymetry for the Oregon coast simulation from 43.25° ($y = 50$ km) to 45.6°N ($y = 335$ km). The bathymetry for $y < 50$ km and $y > 335$ km is the alongshore average appended to make the topography periodic.

The alongshore-uniform channel is 240 km in length in the *y* direction (north to south) and 150 km wide in the *x* direction. The variable bathymetry channel is 380 km in the *y* direction as the bathymetry promotes the presence of larger scales than develop in the uniform alongshore channel case. The horizontal grid resolution in the alongshore direction is 1 km for the alongshore-uniform channel and 1.1 km for the variable bathymetry channel. The resolution in the across-shore direction is stretched for computational efficiency from 400

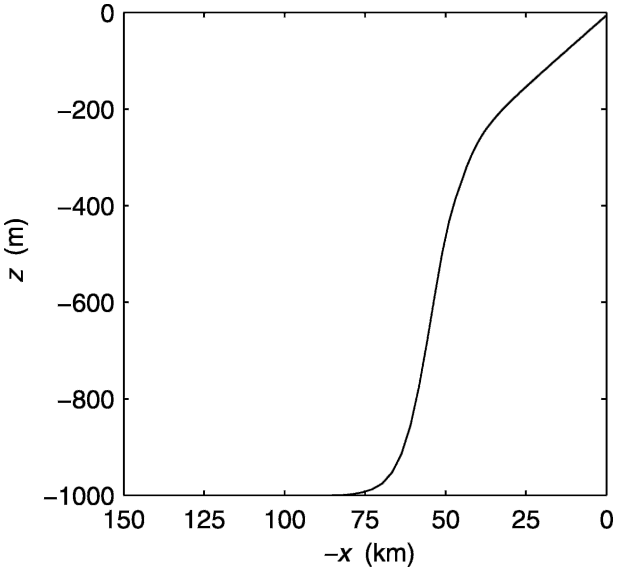

FIG. 3. Bathymetry for the alongshore-uniform domain.

m at the coast to approximately 4 km at the offshore boundary in both domains. In the vertical, 40 sigma levels are used. The bottom depth at the coastal boundary is uniform at 6 m. At the offshore boundary it is 1000 m. The ocean is initialized to be at rest with stratification specified as horizontally uniform. The initial density profile is based on field observations and represents typical summer stratification off the Oregon coast (Fig. 4). It is similar to that used in Allen et al. (1995). The potential density ranges from 23.67 kg m^{-3} at the surface to 27.0 at 1000 m. The maximum initial buoyancy frequency squared N^2 of 0.0007 s^{-2} occurs at approximately 20-m depth. Steady and time-variable wind forcing are both considered in this study. Temporally variable wind stress, which is assumed to be spatially uniform, is obtained from measurements at Newport, Oregon (44.6°N), for July and August 1973. This wind forcing is similar to that previously used in the two-dimensional model simulations in Federiuk and Allen (1995). The steady wind forcing experiments use the time average of the north–south component of wind stress from this record, which is 0.3 dyn cm^{-2} southward (upwelling favorable). Three different cases are studied. The response to 30 days of steady wind in an alongshore-uniform channel (Fig. 3) is studied first (referred to as case 1) to gain a basic understanding of the evolution of the instability. Case 2 involves 60-day integrations with the observed time-variable wind stress in this same domain. A domain with realistic Oregon coast bathymetry (Fig. 2) and 60 days of observed time-variable wind forcing is examined in case 3. For cases 1 and 2, a small perturbation must be introduced into the system for instabilities to develop on the upwelling front. (The same perturbation is applied in case 3 for consistency.) A combination of many spectral components in both x and y directions, with randomly determined phases, are added as a time-independent perturbation to the alongshore wind stress component for the first 2.5 days of the simulation. The maximum magnitude of the perturbation is less than 1% of the alongshore wind stress. Ensembles of simulations, where the wind stress in each member of the ensemble is seeded with different perturbations, are considered in the analysis in both of these cases.

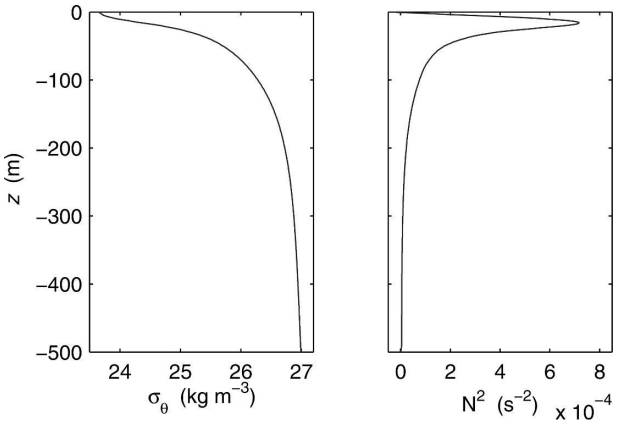

FIG. 4. Initial vertical profiles of potential density and N^2.

The scale of instabilities that develop initially in such experiments have been found to depend sensitively on the model numerics. The third-order upwind advection scheme, which is the default scheme in ROMS, introduces a hyperviscosity that damps grid-scale signals. Alternately, centered second- and fourth-order advection schemes could be utilized. But these tend to artificially amplify the grid-scale signals. Consequently the initial scales of instability generated in model simulations with the third-order upwind scheme tend to be longer than those observed with either the second- or fourth-order centered advection scheme (8 versus 5 km). The magnitude and form of horizontal viscosity and diffusivity can similarly alter the initial observed scale of the instability. Despite these ambiguities regarding the initial scale that the numerical model introduces, the evolution of the system following the initial appearance of disturbances along the upwelling front is quite similar in all cases. Of the advection formulations examined, the third-order upwind scheme results in the most qualitatively realistic solutions, maintaining sharp fronts and complex patterns in the flow field while lim-

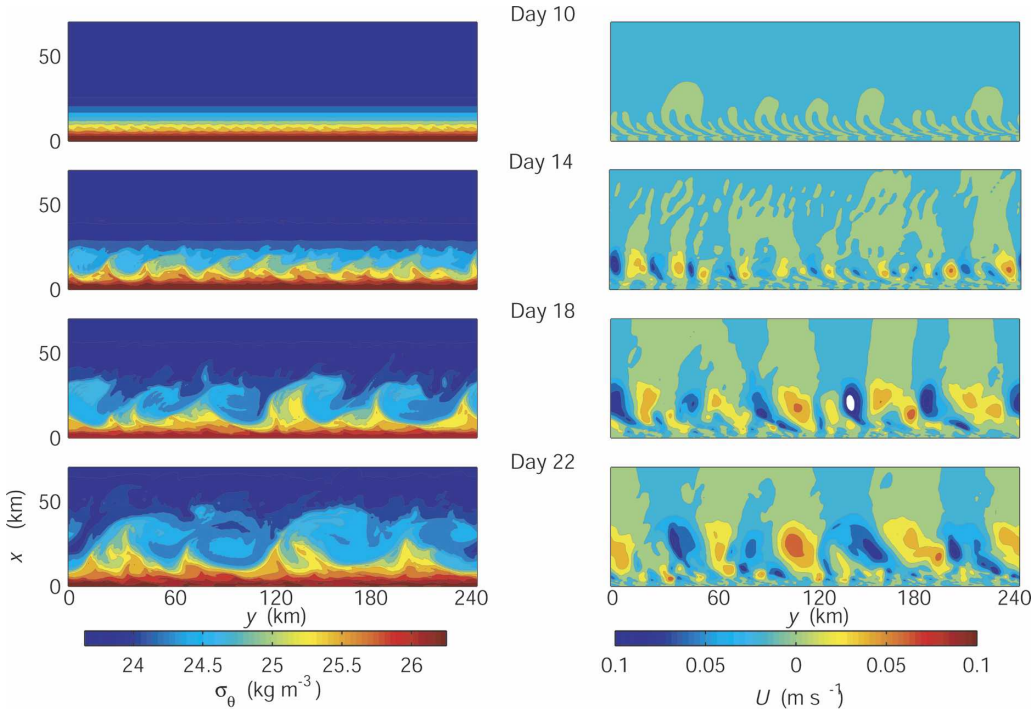

FIG. 5. Contour plots of surface potential density (kg m^{-3}) and depth-averaged across shore velocity U ($m\,s^{-1}$) fields from day 10 through 24 for a case-1 simulation.

iting numerical noise. Consequently, that scheme is utilized for the experiments reported here.

3. Case 1: Instability evolution with steady winds in an alongshore-uniform channel

a. Description of the instability evolution

The steady-wind, uniform-bathymetry simulations (case 1) start from a state of rest. Upwelling develops without indication of instability until approximately day 9 at which point approximately 8-km-scale meanders begin to become discernible along the front. The evolution of the upwelling front from day 10 is depicted in Fig. 5. The surface density field shows 8–10-km-wavelength disturbances developing initially along the front. As the across-shore amplitude of these disturbances becomes larger, the predominant alongshore scale increases significantly to approximately 30 km by day 18 and to greater than 50 km by day 22. An examination of the evolution of wave crests over successive snapshots indicates that adjacent meanders merge into larger-scale features as their across-shore amplitudes increase. Irregularity in the pattern of disturbances develops because of the random distribution of the initial perturbation used in the simulation. The depth-averaged across-shore velocity field U is particularly useful for isolating and quantifying the instability because it is nonzero purely because of their presence. (In an alongshore-uniform upwelling simulation the depth-averaged across-shore velocity is zero.) The across-shore velocity field (Fig. 5) again shows the 8-km-scale instability developing by day 10. The magnitude of the across-shore flow increases as the frontal meanders grow. While energetic larger-scale disturbances develop farther offshore, small scales continue to form in the 15-km region closest to the coast.

The phase of the frontal disturbance propagates southward in the direction of the mean current. Figure 6 shows the depth-averaged across-shore velocity U at a position 12-km offshore as a function of alongshore coordinate and time for one of the case 1 simulations. The sloping red "ridges" (reds and yellows) in the perspective plot demarcate the phase paths of the frontal disturbance. The smallest-scale patterns that appear at the onset of the instability are too weak to be visible in this plot, but the roughly 24-km-scale patterns that succeed them are clearly apparent by day 12. Features on these scales are gradually overwhelmed by larger-scale features by day 20. Over the frontal region as a whole these larger scales remain prominent for the remainder of the simulation but by day 24 they have been dis-

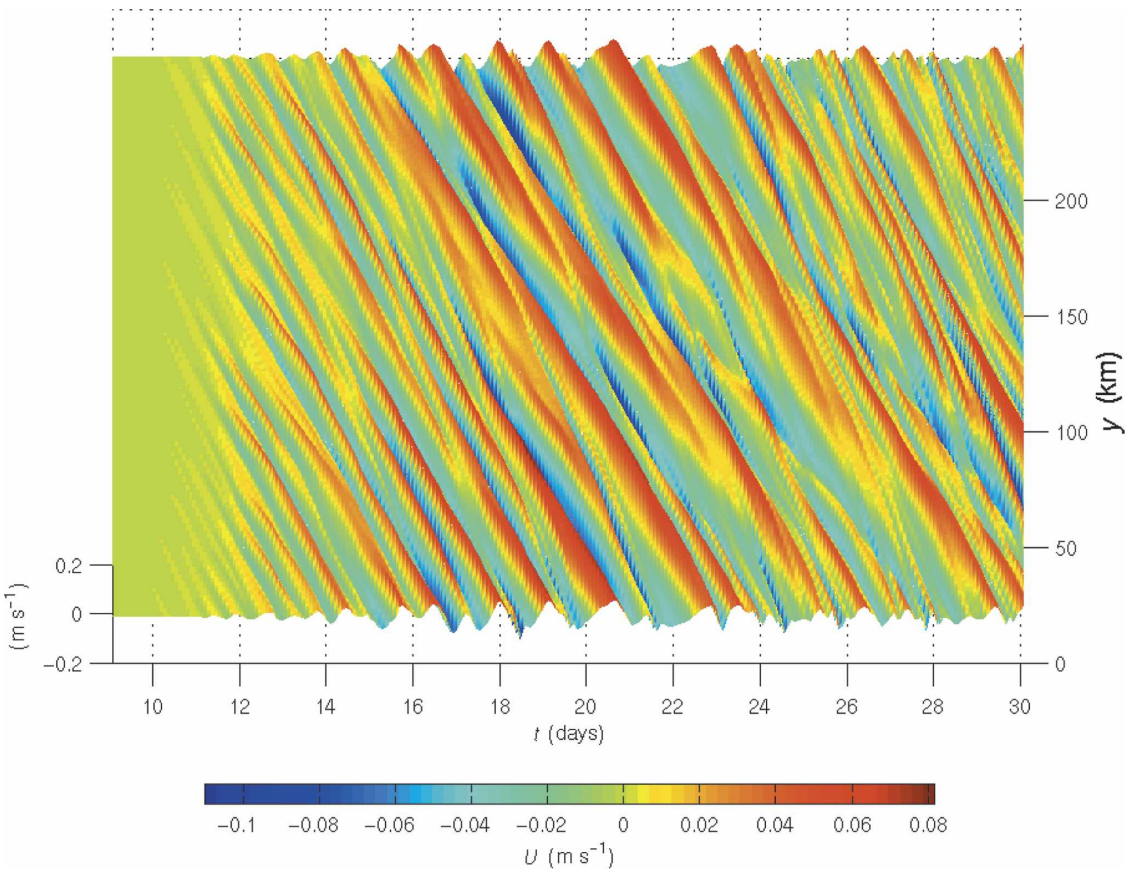

FIG. 6. Perspective plot of depth-averaged across-shore velocity U (m s^{-1}) as a function of alongshore coordinate y and time t along a section 12 km from the coast from a case-1 simulation.

placed farther offshore than the transect 12 km from the coast depicted in Fig. 6, while the shorter-scale patterns persist in this nearshore region. The intersecting paths of long and short wavelength patterns in Fig. 6 indicates that the smaller-scale [O(24 km)] instabilities propagate faster than the larger-scale disturbances (roughly 41 versus 35 cm s^{-1}).

The evolution of the disturbance wavelength can be quantified by spectral analysis of the pattern in the depth-averaged across-shore velocity U. Alongshore wavenumber spectra for U at each across-shore x-grid location are calculated from the instantaneous field. The top panel of Fig. 7 displays the normalized spectra averaged over x as a function of time for one of the case 1 simulations. It shows that the dominant scale of frontal disturbance increases from approximately 8–10 km (λ^{-1} = 0.125–0.1 km^{-1}) to 50 km (λ^{-1} = 0.02 km^{-1}) between days 8 and 22. Although small-scale instabilities continue to develop near shore (Fig. 5), an increasing amount of momentum associated with the disturbance is accumulating at larger scales. The somewhat staircaselike structure of the time evolution of the spectra reflects the abrupt change in wavenumber that occurs as waves merge. The presence of a variety of interacting wavelengths of disturbances prevents a simple interpretation of the shifts in wavelength as being associated with an eddy-pairing-type behavior as discussed in Yamazaki and Peltier (2001). (Indeed in an experiment that was only perturbed at the 8-km scale, a very abrupt shift from 8 to 24 km was observed, suggesting the simultaneous merger of three waves rather than two.)

An alternate interpretation of the scale change is that the favored scale for instability growth is changing as the upwelling circulation evolves. A series of experiments were performed in which the perturbation to the alongshore-uniform state was applied later in the upwelling simulation. Although these experiments cannot exactly mimic the alongshore mean state of the system with instabilities they give some insight into what the fastest growing scales of disturbance are likely to be. The lower five panels of Fig. 7 show the alongshore

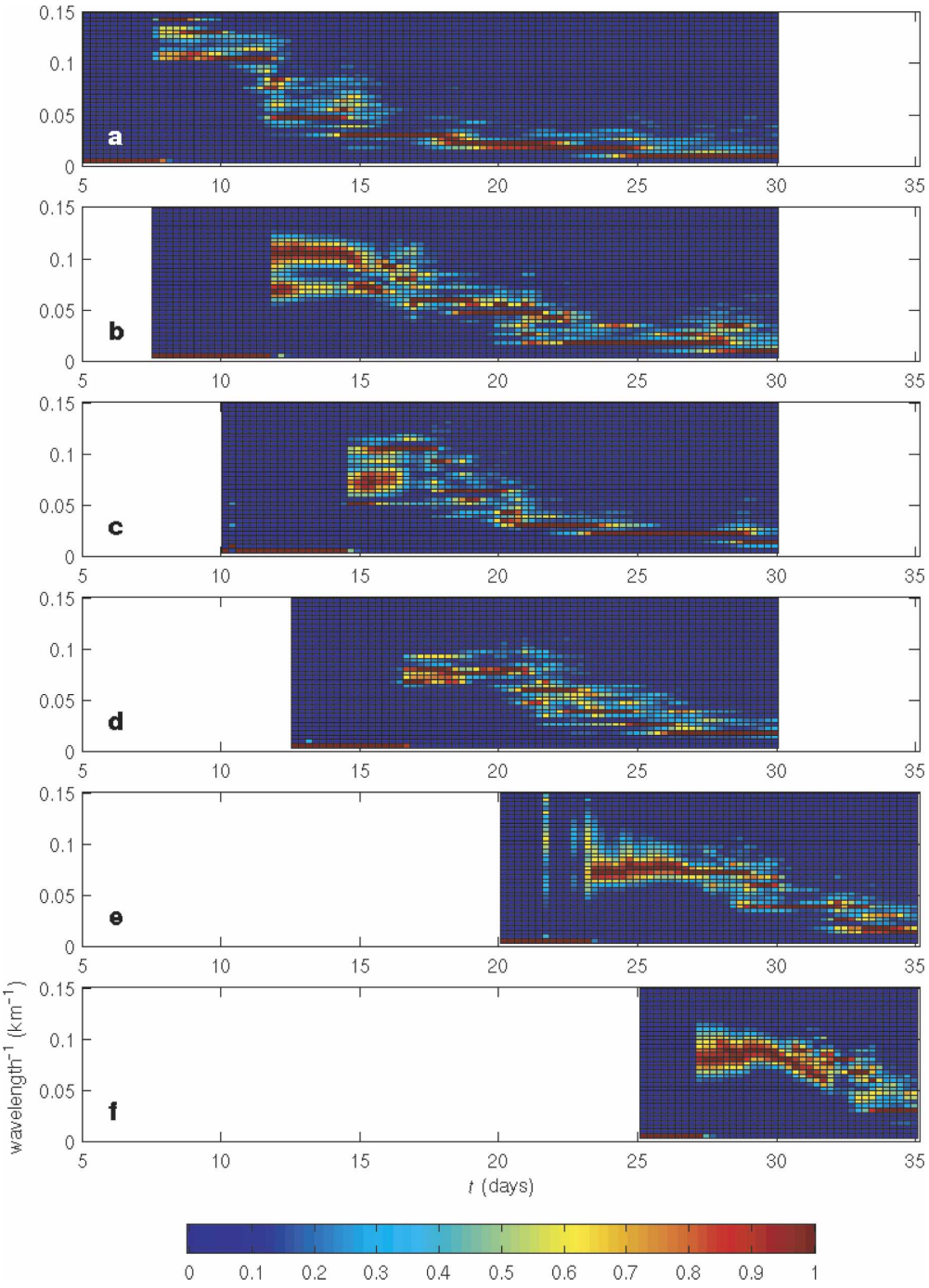

FIG. 7. (a) Dominant alongshore inverse wavelength of frontal disturbances as a function of time t as determined by spectral analysis of the depth-averaged across-shore velocity field u at each across-shore x-grid location for one of the (top) case-1 simulations and for five simulations in which the wind field was perturbed at later times: days (b) 7.5, (c) 10, (d) 12.5, (e) 20, and (f) 25. The spectra are averaged over x. Energy is normalized at each time frame to highlight the change with time. The color palette runs from 0 (dark blue) to 1 (dark red). Red shades indicate spectral peaks near that wavenumber at that time.

wavenumber spectra for simulations that were initially perturbed at day 7.5, 10, 12.5, 20, and 25. (Spectra are plotted only once the total power in the U signal reaches a threshold magnitude, resulting in the blank regions for 1–5 days after the initial disturbance is applied.) There is some indication that by day 15, a disturbance on a scale of roughly 15 km ($\lambda^{-1} \approx 0.067$ km^{-1}) may grow fastest. But in all cases the continued evolution to larger scales appears to progress at a similar rate.

b. Analysis of perturbations about the alongshore average

For further analysis of this system we separate the variables into an alongshore average and a perturbation about that average. We denote the alongshore average by an overbar such that

$$\overline{u} = \frac{1}{L_y} \int_0^{L_y} u \, dy, \tag{1}$$

where L_y is the length of the domain in y. All variables are decomposed—for example,

$$u = \overline{u} + u', \tag{2}$$

where

$$\overline{u'} = 0. \tag{3}$$

In calculating the alongshore average and perturbation quantities in the model, which is formulated in vertical sigma coordinates

$$\sigma = \frac{z - \eta}{H + \eta}, \tag{4}$$

where η is the free surface elevation and $H(x, y)$ is the bottom depth, alongshore variations in sea surface height η are neglected as being relatively small, O(1 cm).

The initial growth and subsequent evolution of the instabilities can be seen clearly from a time sequence of surface fields of the perturbations (Fig. 8). In this figure a set of disturbances is tracked in a frame y' moving at the disturbance phase speed of -34 cm s^{-1} (estimated from Fig. 6). The horizontal structure of the instability evolves rapidly with time. At day 9.25 the surface perturbation potential density field shows a series of disturbances that tilt downstream offshore. At this early stage, the pattern is restricted to the cyclonic side of the jet determined by the alongshore average of the alongshore velocity $\overline{v}$. But by day 10 the disturbance pattern has extended offshore into the region of anticyclonic mean shear and bends back upstream. Shortly thereafter disturbances begin to merge rapidly as these upstream- and downstream-tilted patterns intersect. The merger process does not clearly suggest a pairing mechanism as in Yamazaki and Peltier (2001) but, rather, is more complex. The three small disturbances between y' values of 25 and 50 km, present in Fig. 8 at day 9.25, appear to have merged into a single somewhat skewed, crescent-shaped disturbance by day 12.25.

Further evidence of the evolution of the disturbances to finite amplitude is found by examining the surface perturbation vorticity field $\zeta' = v'_x - u'_y$ divided by the Coriolis parameter f (Fig. 8). The magnitude of the variable ζ'/f is a measure of the local Rossby number in the perturbations. Absolute values near one or higher indicate that nonlinear advective effects are of first-order importance. Appreciable values of ζ'/f are present in the small 8-km-scale fluctuations already on day 9.25. Over the next 4 days, the thin filaments of positive vorticity that slant sharply southward from the coast and curve back northward offshore generally co-occur with the positive surface density perturbations. The progression to larger scales is evident as the filaments stretch in the alongshore direction and intersect each other. In general, the relatively large magnitudes of ζ'/f indicate the importance of nonlinear advective effects in the instability evolution starting as early as day 9.25. Here, as in the spiral eddy study of Eldevik and Dysthe (2002), sharply defined regions of positive perturbation vorticity dominate the surface pattern after day 10.75. Patterns resembling spiral eddies however do not develop in this study, perhaps because of the rapid scale evolution.

To diagnose the sources of the energy for the instability growth, alongshore average and perturbation kinetic energy equations are derived (e.g., Orlanski and Cox 1973). To facilitate physical interpretation, the equations are expressed in Cartesian coordinates. The alongshore-average total kinetic energy equals the sum of the kinetic energy in the average terms and the alongshore average of the kinetic energy in the perturbation; that is,

$$\overline{\mathrm{KE}} = \mathrm{KE}_m + \mathrm{KE}_p, \tag{5}$$

where

$$\mathrm{KE} = \frac{1}{2} \rho_o (u^2 + v^2), \tag{6}$$

$$\mathrm{KE}_m = \frac{1}{2} \rho_o (\overline{u}^2 + \overline{v}^2), \quad \text{and} \tag{7}$$

$$\mathrm{KE}_p = \frac{1}{2} \rho_o (\overline{u'^2} + \overline{v'^2}). \tag{8}$$

The equation for the volume-integrated kinetic energy in the alongshore-averaged flow is

$$\langle \mathrm{KE}_m \rangle_t = -\langle \mathrm{cke} \rangle - g \langle \overline{w} \, \overline{\rho} \rangle + \langle \overline{KF} \rangle + \langle \overline{KD} \rangle. \tag{9}$$

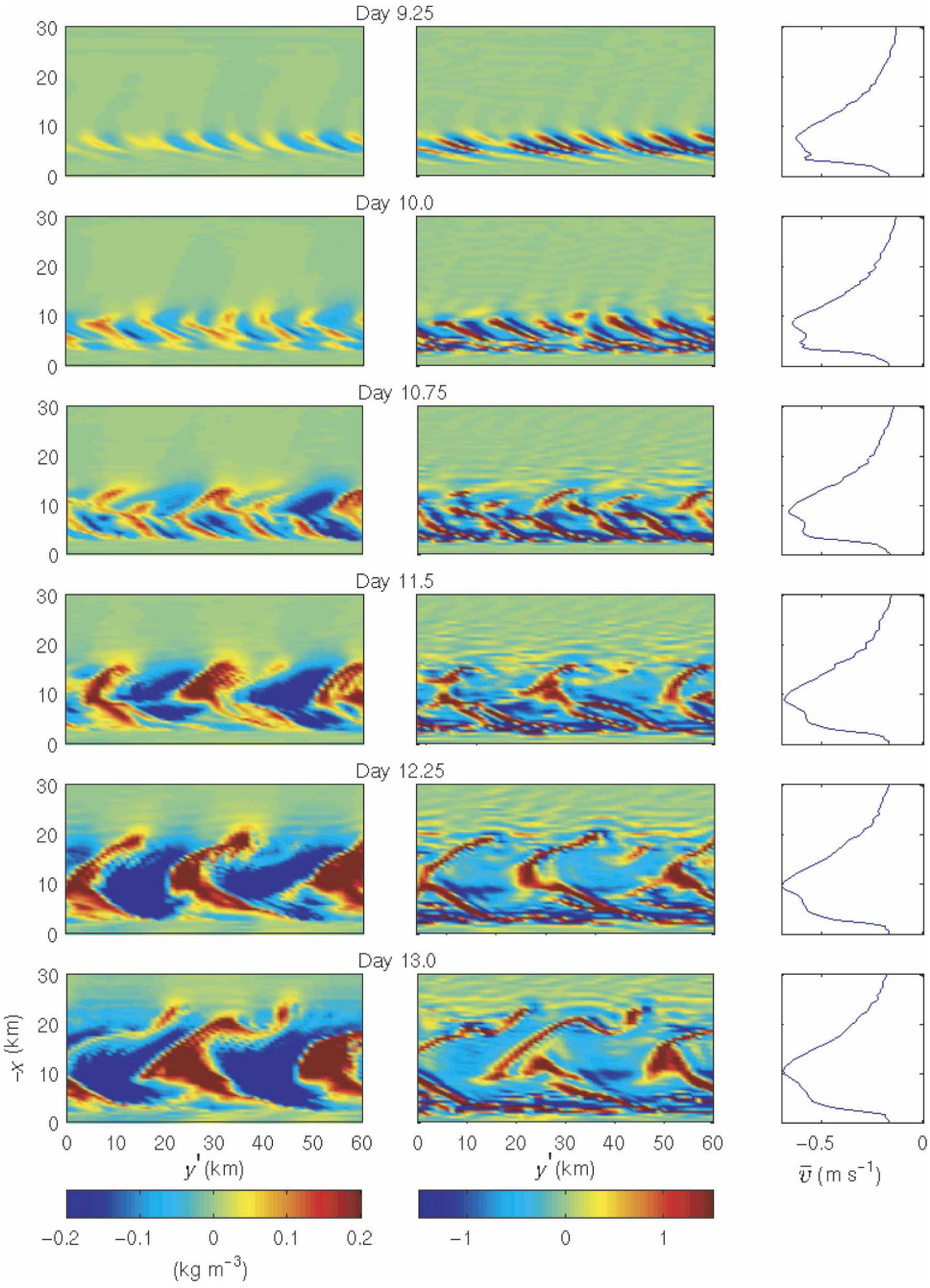

FIG. 8. Contour plots of (left) perturbation surface density fields σ'_θ and (right) perturbation surface vorticity fields $\zeta' = v'_x - u'_y$ divided by the Coriolis parameter f from day 9.25 through 13 for a case-1 simulation and the corresponding alongshore-averaged alongshore current $\bar{v}(x)$. A set of disturbances is tracked in a frame y' moving at the disturbance phase speed of -34 cm s^{-1}.

The equation for the volume-integrated kinetic energy in the perturbations is

$$\langle \mathrm{KE}_p \rangle_t = \langle \mathrm{cke} \rangle + \langle \mathrm{cpe} \rangle + \langle KF \rangle - \langle \overline{KF} \rangle + \langle KD \rangle - \langle \overline{KD} \rangle. \quad (10)$$

In these and the following equations the angle brackets represent volume integrals and the subscripts t, x, and z denote partial differentiation. The kinetic energy transfer term, cke, represents the sum

$$\mathrm{cke} = -\rho_0(\overline{v}_x \overline{u'v'} + \overline{v}_z \overline{w'v'} + \overline{u}_x \overline{u'u'} + \overline{u}_z \overline{w'u'}). \quad (11)$$

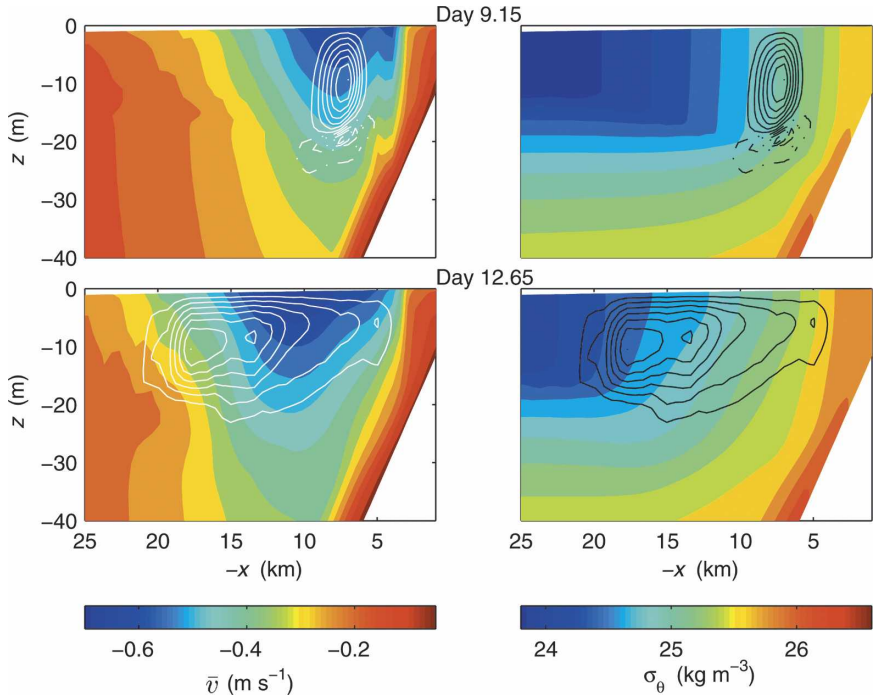

FIG. 9. (left) Alongshore-average alongshore velocity $\bar{v}$ with cpe (12) overlaid in white for two times during the early development of the instability. (right) The alongshore-average density field with cpe overlaid in black (for clarity). For cpe solid contours are positive and dashed contours are negative.

The transfer of potential energy to perturbation kinetic energy term cpe is

$$\text{cpe} = -\overline{gw'\rho'}. \tag{12}$$

Here *KF* represents the rate of change of kinetic energy associated with the surface and bottom stresses, and *KD* represents the dissipation due to vertical mixing processes. The constant reference density $\rho_o = 1000$ kg m^{-3} and g is the acceleration of gravity. The sum of terms in cke (11) is calculated in the model from an equivalent sum of terms in sigma coordinates. The potential energy transfer term, cpe, explicitly involves the Cartesian coordinate vertical velocity w, which is calculated consistently from the variables in sigma coordinates.

An equation for the rate of change of volume-integrated potential energy can be derived as

$$\langle \text{PE}_m \rangle_t = g\langle \overline{w}\,\overline{\rho} \rangle - \langle \text{cpe} \rangle + \langle \overline{RD} \rangle, \tag{13}$$

where

$$\text{PE} = g\rho(z - z_o), \tag{14a}$$

$$\text{PE}_m = g\bar{\rho}(z - z_o), \quad \text{and} \tag{14b}$$

$$\text{PE}_p = 0, \tag{14c}$$

and *RD* represents the change in potential energy due to vertical mixing processes.

The onset of the instability can be characterized by examining the increase in magnitude of the various perturbation kinetic energy source terms as the instabilities first develop. The initial growth of the instability is associated with a rapid increase in cpe indicative of baroclinic instability (Fig. 9). On day 9.15 cpe builds in a 20-m-deep, 5-km-wide region approximately 8 km from the coast, roughly centered on the maximum in the alongshore-averaged alongshore velocity field. Over the next 3.5 days, the region of strong conversion of potential to perturbation kinetic energy stretches offshore, remaining primarily limited to the top 20 m of the water column, with the maximum conversion occurring increasingly offshore of the maximum in the alongshore-averaged alongshore jet. This maximum advances offshore faster than the alongshore-averaged density front as well. This offshore movement of the region of high cpe at a rate faster than the rate of offshore advection of the upwelling front and jet suggests that the instabilities rapidly reach a stage of nonlinear development in which their direct association with a "background state" is unclear.

The mechanism for the development of the baroclinic instability is apparent in alongshore-depth section

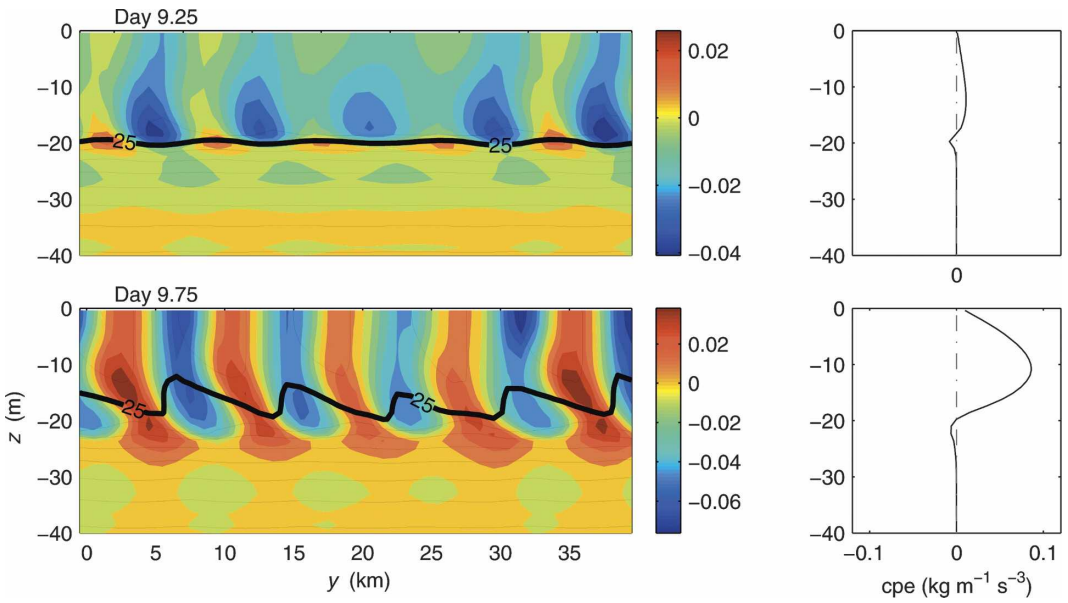

FIG. 10. (left) Potential density (black contours) and across-shore velocity (color contours, m s^{-1}), for a 60-km alongshore section 8 km from the coast, on days 9.25 and 9.75 for a case-1 simulation. Note that offshore velocities are negative in this figure and directed into the page. The contour interval for potential density is 0.1 kg m^3, with a heavy contour used for $\sigma_\theta = 25.0$ kg m^3. The horizontal axis is being translated at the alongshore average v velocity at 20-m depth to follow the features in time. (right) The cpe depth profile at this section.

contour plots of density and across-shore velocity (Fig. 10). These are plotted at an offshore position near the core of positive cpe on day 9.15 in Fig. 9. At day 9.25, a pattern of onshore/offshore flow is visible in 8–10-km-wide cells, alternately located above and below the base of the mixed layer. The deeper onshore flow cells advect lighter water shoreward across the front into denser water, while the shallow offshore cells advect dense upwelled water offshore. Vertical velocities are predominantly positive in the lower-density onshore flows and negative in the higher-density offshore flows consistent with movement of water parcels into the "wedge of instability" (Pedlosky 1987, his section 7.6). The net result of this process is quantified by the positive values of cpe in Fig. 10 that clearly show the release of potential energy in the top 20 m of the water column. The alongshore density gradients that the across-front advection patterns generate quickly become asymetric (Fig. 10). While in some regions the thermal wind balance of the across-shore velocity indicates enhanced onshore/offshore flow consistent with instability growth, it does not account for the full vertical structure of the across-shore velocity. In particular, the vertical structure is strongly ageostrophic where sharp positive along-channel density gradients develop and the horizontal circulation is strongly cyclonic.

As the instability grows, the pycnocline breaches the surface forming an upwelling front. Regions where the top of the pycnocline has been stretched upward to the surface correlate with where the upwelling front meanders farthest offshore. By day 9.75, intense offshore velocities are beginning to become visible at the surface, associated with these across-shore meanders. By day 11 (not pictured) the surface circulation is more intense than that at the base of the mixed layer and the further development of the instabilities is most visible in horizontal surface maps.

To help to identify how kinetic and potential energy in the alongshore average flow are exchanged with the kinetic energy in the perturbations the time and space dependence of the potential energy transfer term, cpe, and of the sum of the kinetic energy transfer terms, cke, are examined. The top panel of Fig. 11 displays the volume integrals of these two fields for one of the case-1 ensemble members. Contour plots of the depth integrals of cke and cpe,

$$\mathrm{cKE} = \int_{-H}^{\eta} \mathrm{cke}\, dz \quad \text{and} \tag{15}$$

$$\mathrm{cPE} = \int_{-H}^{\eta} \mathrm{cpe}\, dz, \tag{16}$$

as a function of time t and across-shore distance x and across-shore sections of cpe and cke at day 14 and day 20 for the same case-1 simulation are also shown in Fig. 11. The increasing positive value of $\langle \mathrm{cpe} \rangle$ between days

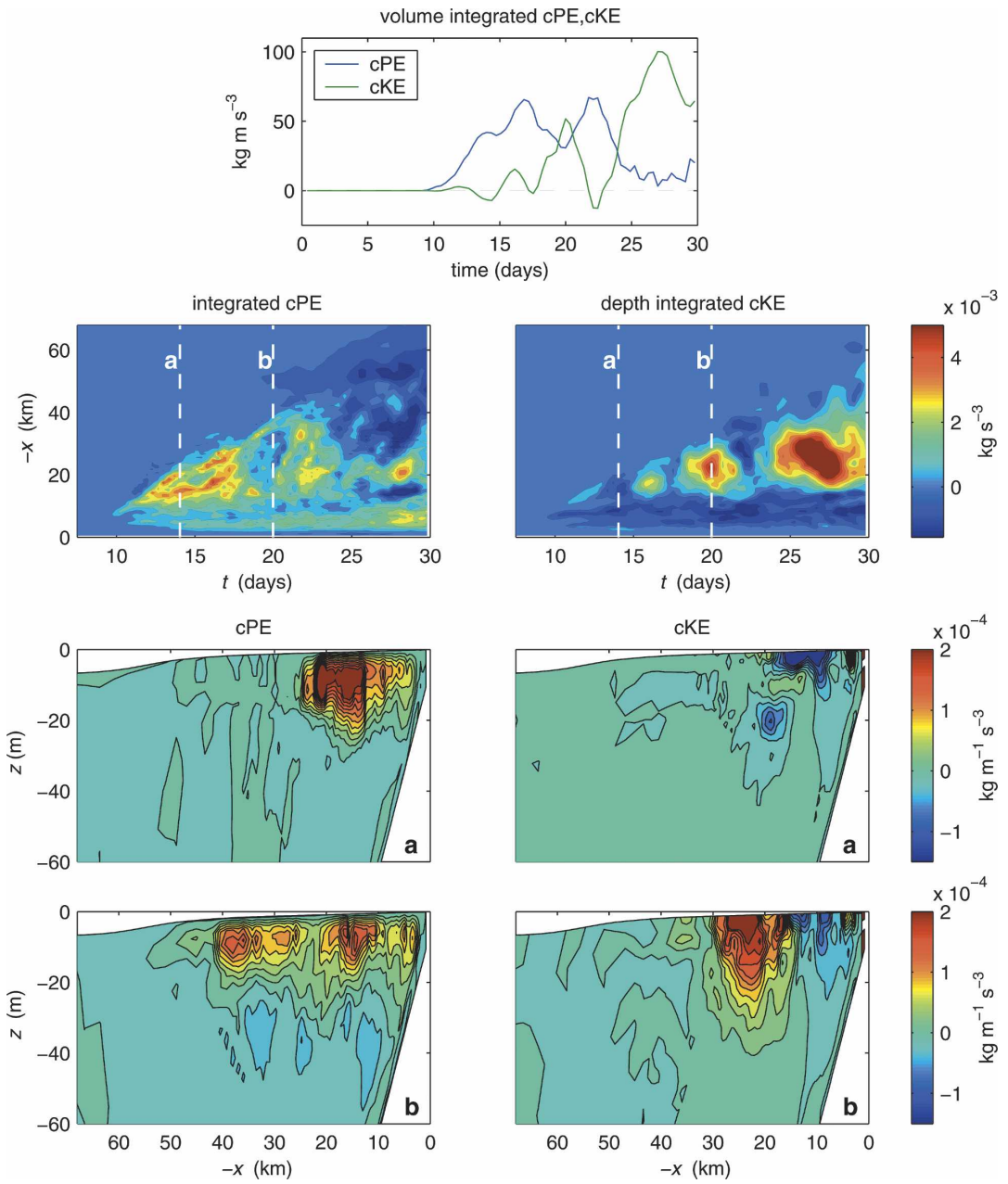

FIG. 11. (top) Volume integrals, (middle) depth integrals contoured as a function of time t and across-shore position x and (bottom four panels) x–z sections of the perturbation kinetic energy conversion terms cpe (12) and cke (11) for a case-1 simulation. Units are kilograms per second cubed for the depth integrals and kilograms per meter per second cubed for the sections. Sections are for (a) day 14 and (b) day 20.

10 and 17 shows that the initial development of the instability derives energy by transfer from the density field (as indicated previously by the cpe plots of Fig. 10). Subsequent to this there are intermittent positive bursts in ⟨cke⟩, which co-occur with decreases in ⟨cpe⟩. This same general pattern appears in each of the 10 randomly perturbed simulations performed for case 1. However, both the timing and the duration of the bursts vary broadly among the ensemble members. The variations of cPE and cKE indicate the across-shore dependence of the contributions to ⟨cpe⟩ and ⟨cke⟩. The initial growth of cPE during days 10–17 occurs in the frontal region 10–25 km offshore. The depth distribution of cpe at day 14 shows that energy from the density field is being released by the overturning of the front in the top 30 m of the water column. At approximately day 20,

baroclinic conversion to perturbation kinetic energy cPE has diminished, but transfer from the mean kinetic energy field cKE has increased significantly. The transfer of energy cKE from the mean kinetic energy field occurs predominantly in a band approximately 15 km wide across shore and 40 m deep at this time. It develops on the offshore side of the alongshore average position of the jet maximum v velocity.

The question may be asked whether the periods of sharply increasing ⟨cke⟩ are associated with a barotropic instability on the evolved "background state." The intermittent increases in ⟨cke⟩, however, were not found to be related to any clear patterns in the evolution of the alongshore-averaged fields. Several experiments were performed that were initialized with the alongshore-averaged fields from case-1 simulations at times immediately preceding a strong increase in ⟨cke⟩. None showed a tendency for large ⟨cke⟩ for at least 10 days subsequent to this initialization, while all showed the familiar increases in ⟨cpe⟩ and development of 8–10-km-scale instabilities. These results suggest that the large values of ⟨cke⟩ result from wave–wave rather than wave–mean flow interactions. Figure 12 shows ⟨cpe⟩ and ⟨cke⟩ (top panel) for an ensemble member with a particularly strong burst of kinetic energy conversion. The lower panels show the evolution of the surface density field as ⟨cke⟩ first increases and then rapidly diminishes. Coincident with the increase in ⟨cke⟩ near day 23, waves of roughly 40-km scale present at day 19 coalesce into large 80-km wavelength disturbances that extend nearly 50 km offshore. Rather quickly, however, smaller-scale patterns begin to reemerge as is visible predominantly toward the northern end of the domain by day 25.

The equation for the rate of change of alongshore-averaged alongshore momentum is

$$\bar{v}_t = -(\bar{u}\,\bar{v})_x - (\overline{u'v'})_x - (\overline{w}\,\bar{v})_z - (\overline{w'v'})_z - f\bar{u} + \overline{MD}, \tag{17}$$

where MD represents mixing terms. Modification of the mean alongshore momentum by the perturbation field is associated with the terms

$$m_f = -(\overline{u'v'})_x - (\overline{w'v'})_z. \tag{18}$$

Figure 13 shows the depth integral of m_f,

$$M_f = \int_{-H}^{\eta} m_f\,dz = -\frac{\partial}{\partial x}\left(\int_{-H}^{\eta} \overline{u'v'}\,dz\right), \tag{19}$$

as a function of x and t, averaged over an ensemble of ten simulations, along with the analogous plots for cPE and cKE. The center of the alongshore jet as estimated from the alongshore-averaged surface v is overlaid. Recall that negative values of M_f, contributing to $\bar{v}_t < 0$, act to increase the strength of the southward alongshore current. Shortly after the onset of the instabilities, the perturbations act to accelerate the flow southward in an increasingly broad band on the offshore side of the jet maximum. Onshore of the jet maximum southward-directed momentum is lost from the alongshore average. The region of positive ensemble averaged cKE that develops after day 15 coincides with the region on the offshore side of the jet maximum in which the disturbances are accelerating the southward flow.

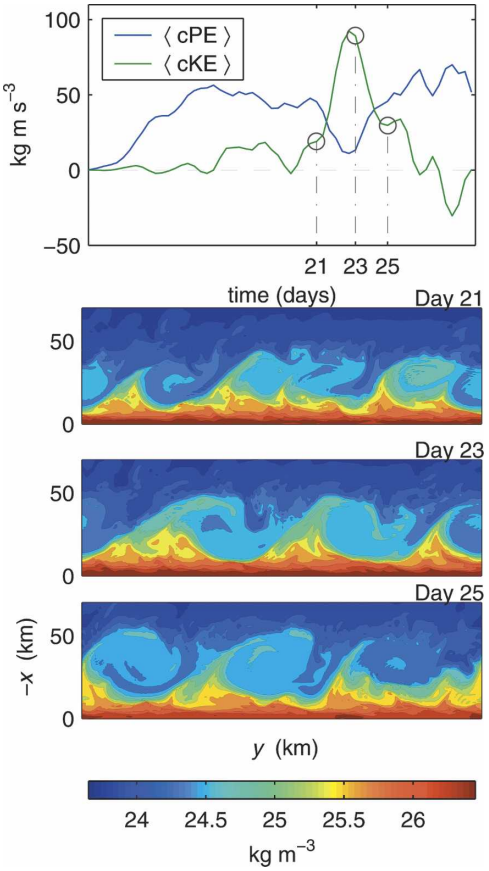

FIG. 12. (top) Volume integrals of the perturbation kinetic energy conversion terms cpe (12) and cke (11) for a case-1 simulation and corresponding contour plots of (lower panels) the surface density field days 21, 23, and 25.

The equation for the rate of change of the alongshore-averaged density is

$$\bar{\rho}_t = -(\bar{u}\,\bar{\rho})_x - (\overline{u'\rho'})_x - (\overline{w'}\,\overline{\rho'})_z - (\overline{w'\rho'})_z + \overline{DD}, \tag{20}$$

where DD represents the mixing terms. Modification of the mean density by the perturbation is associated with the terms

$$d_f = -(\overline{u'\rho'})_x - (\overline{w'\rho'})_z. \tag{21}$$

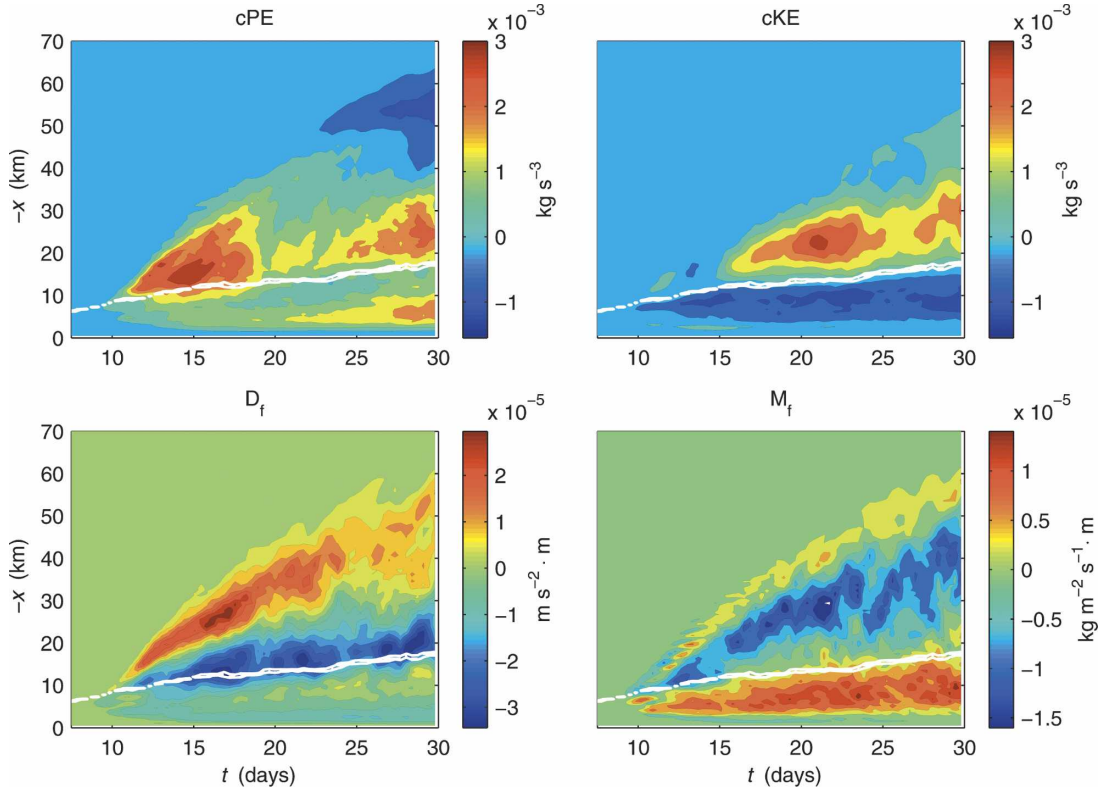

FIG. 13. Depth integrals contoured as a function of time t and across-shore position x; (top left) cPE (16), (top right) cKE (15), (bottom left) D_f (22), (bottom right) M_f (19) calculated from an ensemble average of 10 case-1 simulations. The maximum in the southward-directed ensemble-averaged alongshore-averaged alongshore momentum, representing the center of the coastal jet, is overlaid in white.

The depth integral of d_f,

$$D_f = \int_{-H}^{\eta} d_f \, dz = -\frac{\partial}{\partial x}\left(\int_{-H}^{\eta} \overline{u'\rho'} \, dz \right), \qquad (22)$$

as a function of x and t is also shown in Fig. 13. The instabilities lead to an increase in density offshore and a decrease nearer to shore from the onset of their evolution. The jet maximum falls near the onshore edge of the region of negative D_f. Despite the rather steady pattern depicted in Fig. 13 for the ensemble average, density is fluxed most strongly in the cross-channel direction in conjunction with the bursts of positive ⟨cke⟩ (visible in Fig. 11). The evolution of the surface density fields also show this effect as the large-scale frontal disturbances that develop during the periods of high ⟨cke⟩ deflect the density front farther offshore (Fig. 12).

4. Case 2: Instability evolution with variable winds in an alongshore-uniform channel

A temporally variable wind stress can influence the flow structure on a time scale comparable to that of the instability growth. To investigate the effects of time-dependent forcing on the instability development, a Newport, Oregon (44.6°N), wind data record from July and August 1973 was used in case 2 to force the same alongshore-uniform model domain for a period of 60 days. A time series of the alongshore component of the wind stress over the 60-day period is displayed at the top of Fig. 14. Several upwelling events occur during this period. The tail end of an event occurs at the very start of the record. A strong, brief wind pulse develops between days 13 and 17. And a more moderate, longer upwelling event occurs between days 26 and 40. The first visible indication of a growing disturbance on the front develops by day 12 at approximately a 15-km wavelength in response to the upwelling that occurred during the first several days of the simulation (Fig. 14). The cross-shore extent of the disturbances are amplified in response to the strong wind pulse centered on day 15. Scales along the front increase significantly over the following 10 days to reach approximately a 60-km scale. By day 29, several days after the onset of upwelling winds, these large-scale disturbances stretch far offshore and smaller wavelength patterns reemerge

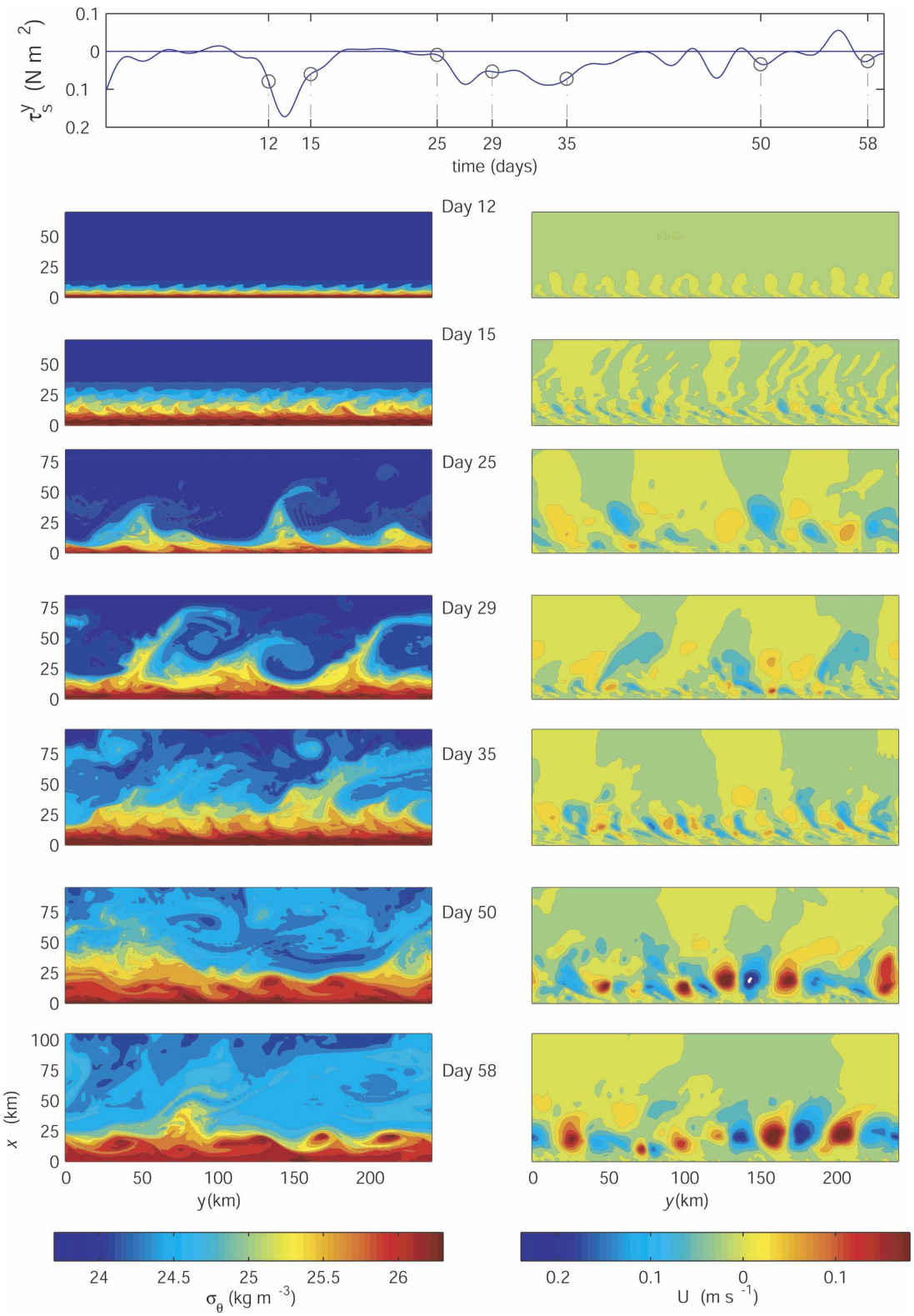

FIG. 14. Contour plots of the surface potential density (kg m^{-3}) and depth-averaged across-shore velocity U (m s^{-1}) fields from selected days between 12 and 58 from a case-2 simulation with time-variable wind stress (shown at the top).

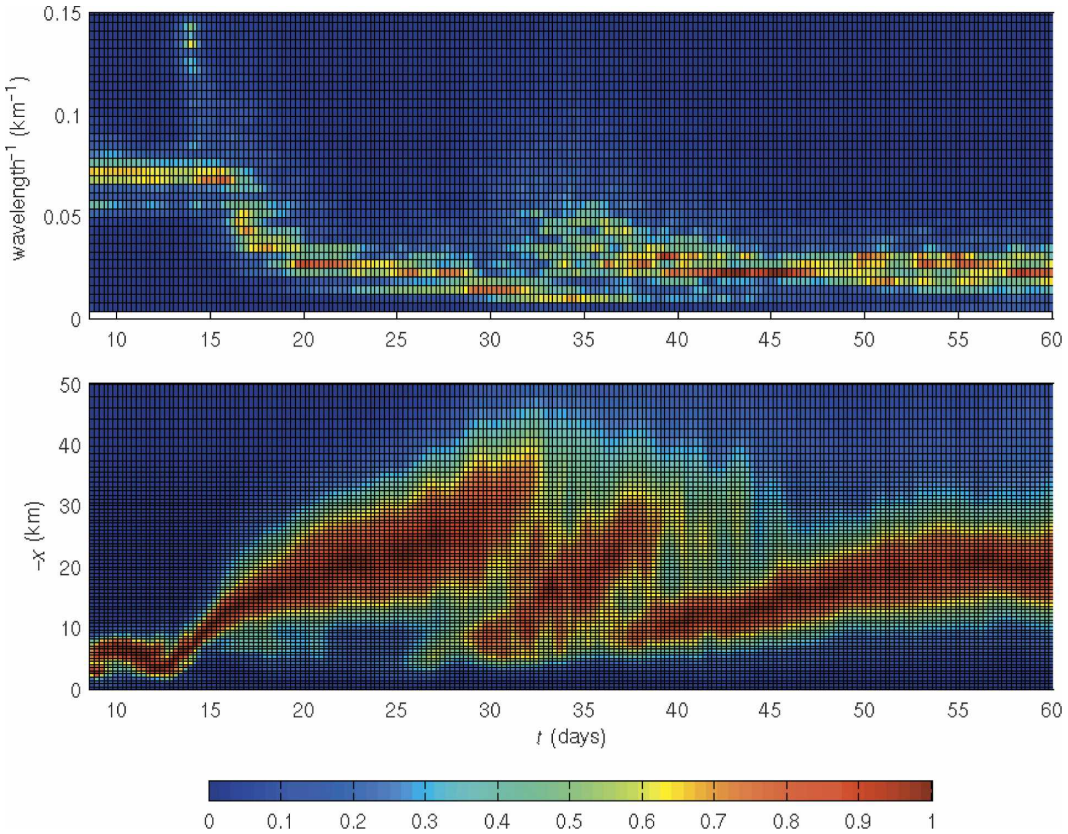

FIG. 15. (top) Dominant alongshore inverse wavelength of frontal disturbances as a function of time t and (bottom) instability energy as a function of t and across-shore coordinate x as determined by spectral analysis of the depth-averaged across-shore velocity field at each across shore x grid location for an ensemble of five case-2 simulations. In the top panel the spectra are averaged over x. In both panels, energy is normalized at each time frame to highlight the change with time.

close to the coast in the most recently upwelled portion of the front. The shorter-scale disturbances grow during the upwelling wind event replacing the larger-scale structure by day 35. For the remainder of the simulation, during which the winds are moderate and variable, a complex mixture of scales is visible. The reappearance of the small scales with the second major upwelling event between days 26 and 40, and the sustained presence of these scales through the rest of the simulation suggest that the upwelling wind pulses are playing an important role in the generation of flow conditions susceptible to these instabilities.

The rate of change of alongshore scale can again be quantified by spectral analysis of the alongshore variation in the depth-averaged across-shore velocity field. As in Fig. 7, Fig. 15 shows the across-shore-averaged energy distribution as a function of alongshore wavenumber and time in the top panel. (Here the energy is normalized separately for each time.) The earliest detectable scale of disturbance is 15 km ($\lambda^{-1} \approx 0.067$ km^{-1}) in contrast to the 8–10-km scale observed in case 1. This is likely due to the differences in stratification and alongshore velocity produced by the time-variable wind forcing.

The predominant disturbance scale increases rapidly following the strong upwelling event between days 13 and 17 (Fig. 15). The second upwelling event reintroduces smaller alongshore-scale disturbances as the predominant scale drops from 60 km ($\lambda^{-1} \approx 0.0167$ km^{-1}) to 25 km ($\lambda^{-1} \approx 0.04$ km^{-1}) between days 33 and 36. Larger scales subsequently develop, and a mixture of scales is apparent during the period of variable winds between days 40 and 60.

The larger-scale patterns that are associated with the evolution of the instabilities from the earlier upwelling event generally appear offshore of the smaller-scale, "younger" instabilities associated with the most recent event. In the lower panel the distribution of the total energy in the spectra as a function of across-shore coordinate x and time t is displayed. The bottom panel shows that these smaller scales originate within 10 km of the coast, well shoreward of the maximum in the

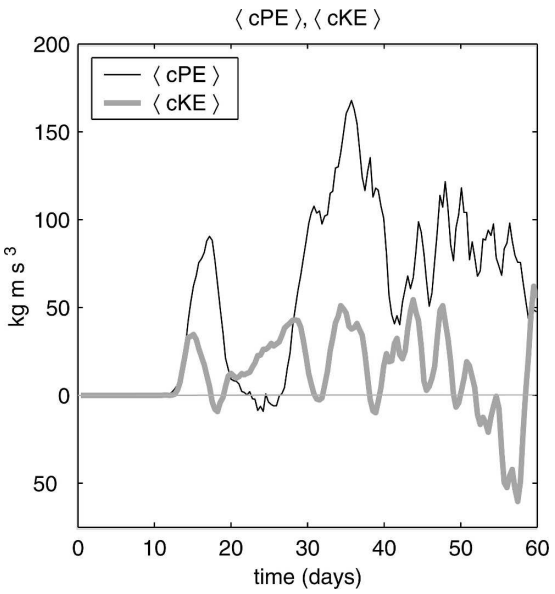

FIG. 16. Volume integrals of the perturbation kinetic energy conversion terms cpe (12) and cke (11) for an ensemble of five case-2 simulations.

alongshore-mean jet velocity, rapidly extend offshore, and dissipate by day 38.

Terms of the perturbation kinetic energy equation (10) again illustrate the primary energy conversion processes occurring in this system. The volume and depth integrals of the baroclinic energy conversion term cpe (12) and the sum of the kinetic energy conversion terms cke (11) are displayed in Fig. 16 and the top two panels of Fig. 17, respectively. These fields are obtained as averages over an ensemble of five simulations seeded with different noise. The initial growth of the instability again correlates with a positive transfer of energy from the potential energy field ⟨cpe⟩. During the period of relaxed winds between day 22 and 28, the potential energy conversion term diminishes significantly. But with the onset of the second strong upwelling-favorable wind event (day 26), potential energy conversion to perturbation kinetic energy develops again. This suggests that the upward distortion of the isopycnals that the upwelling winds cause promote conditions favorable for instability growth. Indeed x–z sections of

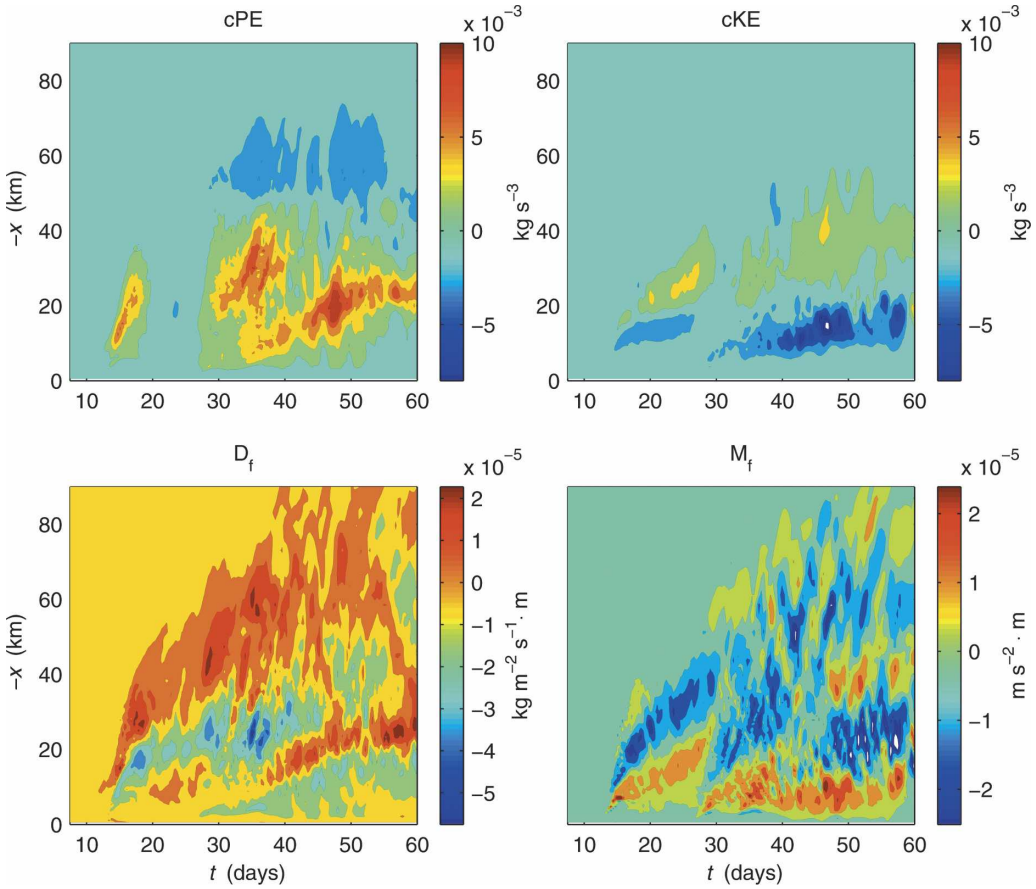

FIG. 17. Depth integrals contoured as a function of time t and across-shore position x; cPE (16), cKE (15), D_f (19), and M_f (22) for an ensemble of five case-2 simulations.

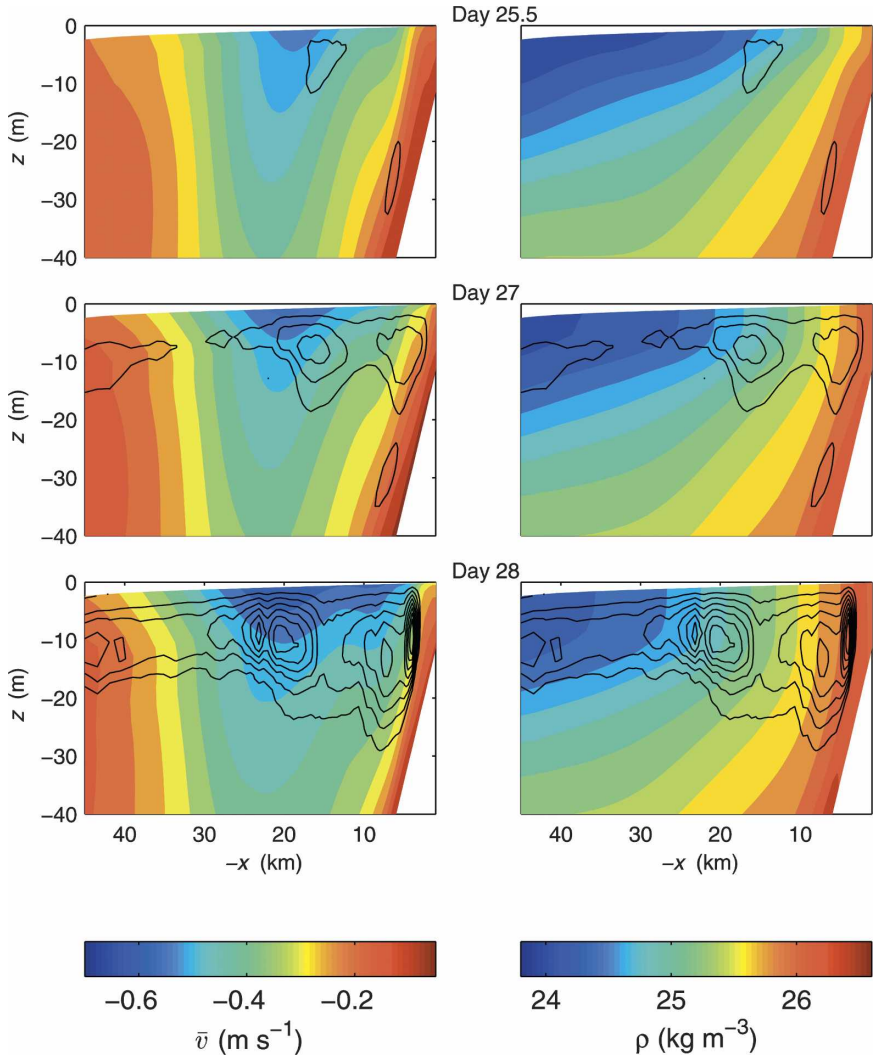

FIG. 18. (left) Alongshore-averaged alongshore velocity v with cpe (12) overlaid for three times during redevelopment of smaller-scale disturbances along the front (days 25.5, 27, and 28) from an ensemble of five case-2 simulations. (right) Alongshore-averaged density field with cpe overlaid. For cpe, solid contours are positive and dashed contours are negative. The contour interval for cpe is 2.5×10^{-5} kg m^{-1} s^{-3}.

alongshore average $\bar{v}$ and $\overline{\sigma}_\theta$ with cpe overlaid in Fig. 18 reveal a rapid intensification of the potential energy conversion in the frontal region as the jet strengthens and the isopycnals steepen in response to the upwelling-favorable wind. On days 29–37 during this second strong upwelling event, large values of cPE occur farther offshore 20–40 km from the coast in the strengthening coastal jet.

Production of perturbation kinetic energy via transfer from the kinetic energy of the alongshore mean flow occurs in case 2 similarly to in the steady wind simulations (Fig. 16). The principle response of the system to the upwelling-favorable wind events is a baroclinic instability evidenced by large values of ⟨cpe⟩; ⟨cke⟩ shows intermittent increases in magnitude. In each ensemble member of case 2, the period of relaxed wind between days 18 and 26, was a period in which ⟨cpe⟩ diminished and ⟨cke⟩ increased. After day 26, however, there was no clear correlation between wind relaxation and positive ⟨cke⟩ events. The periods of positive perturbation kinetic energy transfer ⟨cke⟩ on days 20–30 and 30–50 are associated with positive cKE offshore while nearshore cKE remains negative (particularly from days 30 through 60).

The lower two panels of Fig. 17 display x–t sections of M_f and D_f obtained as averages over the ensemble of five case-2 simulations. The effect of the individual wind events is distinguishable in both fields. A region of

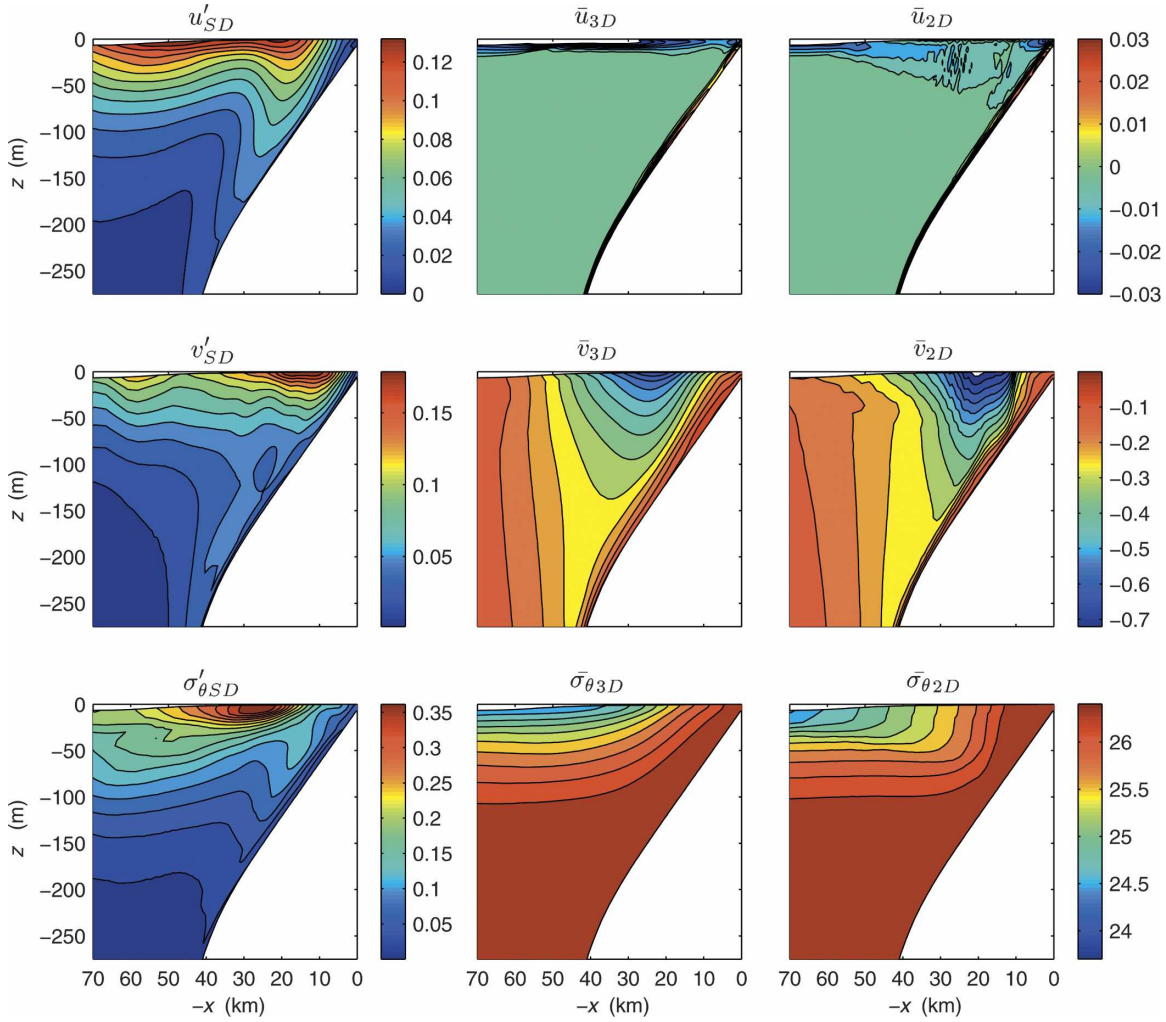

FIG. 19. Time average between days 30 and 60 of the alongshore-averaged $\bar{u}$, $\bar{v}$, and $\bar{\sigma}_\theta$ and the time average between days 30 and 60 of $(\overline{u'^2})^{1/2}$, $(\overline{v'^2})^{1/2}$, and $(\overline{\sigma'^2_\theta})^{1/2}$, which we denote as u'_{SD}, v'_{SD}, and $\sigma'_{\theta\mathrm{SD}}$, respectively, for case 2–3D and case 2–2D.

negative M_f expands offshore in response to the wind pulse starting on day 13 while a comparable patch of positive M_f broadens near shore similar to the behavior in case 1 (Fig. 13). The expansion of this pattern offshore continues through day 28 despite the relaxation of the wind. With the onset of the next upwelling wind event, this pattern is largely disrupted and new patches of positive and negative M_f develop near shore, expanding offshore rapidly. Late in the simulation it appears that the remnants of earlier wind events may determine the distribution of positive and negative M_f well offshore. The D_f field shows a similar responsiveness to each wind event and appears to maintain a history of previous events in the offshore patterns.

It is useful to assess the net effect of the instabilities on the time-averaged circulation in case 2 by comparison with the comparable two-dimensional (x–z section) simulation in which instabilities do not develop. This case-2–2D simulation is attained by rerunning the model with a setup identical to case 2–3D but with no perturbation applied to the wind field. The result of the case-2–2D simulation remains alongshore uniform for all times. In Fig. 19 we plot the time average between days 30 and 60 of the alongshore-averaged $\bar{u}$ and $\bar{v}$ velocity components and the density field $\bar{\sigma}_\theta$ for case 2–3D and case 2–2D. When instabilities are present in case 2–3D, the time-averaged offshore flow in the surface layer is confined to shallower depths. The isopycnals are much less steeply sloped and correspondingly the time mean alongshore jet is shallower and broader. To help quantify at what across-shore location and depth the instabilities are introducing alongshore variability in the system we also plot (Fig. 19) the time average of the alongshore standard deviations about

the alongshore means—that is, the time average between days 30 and 60 of $(\overline{u'^2})^{1/2}$, $(\overline{v'^2})^{1/2}$, and $(\overline{\sigma_\theta'^2})^{1/2}$, which we denote as u'_{SD}, v'_{SD}, and $\sigma'_{\theta SD}$, respectively. The variability in all of these fields is surface intensified with the largest values at the surface and with generally small values below 60-m depth. Maximum values for u'_{SD} are found at approximately 20 and 60 km offshore, while the largest values of v'_{SD} occur at 20 km from the coast. The across-shore structure of $\sigma'_{\theta SD}$ shows the largest values at about 25 km offshore, with weaker fluctuations extending to greater depths offshore 60 km from the coast.

5. Case 3: Instability evolution with variable winds in a channel with realistic Oregon coast bathymetry

It has been established, in previous modeling studies of circulation on the central Oregon shelf (Oke et al. 2002a,b), that the offshore position of the upwelling front tends to vary with the bathymetry, the major feature of which is a bank (Heceta Bank) approximately 100 km in alongshore length that juts approximately 50 km offshore. It is of interest here to determine if the scales of frontal instabilities observed in the alongshore-uniform channel simulations still appear in the presence of realistic alongshore-variable bathymetry and what interaction there is between instabilities and the frontal deflections associated with the bathymetric effects. To pursue that, in case 3 the alongshore-uniform bathymetry is replaced with variable bathymetry based on data from the Oregon coast (Fig. 2). Heceta Bank is located between $y = 125$ km and $y = 225$ km. Time-variable wind forcing, as in case 2, is applied.

Figure 20 displays fields of surface density for different times during the case-3 simulation. The alongshore component of the wind record is included at the top of Fig. 20. Frontal disturbances are excited early in the simulation, associated with the initial brief upwelling event that occurs at the very start of the wind record. After the first strong upwelling event on days 13–16, frontal instabilities of roughly 24-km scale are present. As in case 2, small-scale instabilities $O(15$ km) reappear after the onset of the sustained wind event beginning on day 26. These are most visible in the southern 100 km of the domain where prior to the wind event frontal deflections are weakest. By day 20, the front is visibly deflected offshore along the northern side of Heceta Bank. Frontal deflections are accentuated over the bank as large-amplitude meanders associated with the instabilities are forced to propagate offshore then sharply back onshore, along the curved frontal path established by the topographic effects. A broad, $O(100$ km) alongshore scale, region of complex surface circulation develops over the bank and its southern flank in which the meanders associated with the instabilities become highly contorted. An example of the result of the interaction of the instabilities with the topography-induced frontal curvature can be observed between days 20 and 38. The density fields show a large-scale $O(60$ km) deflection of the front develops at the bank by day 20. Over the southern portion of the bank, the

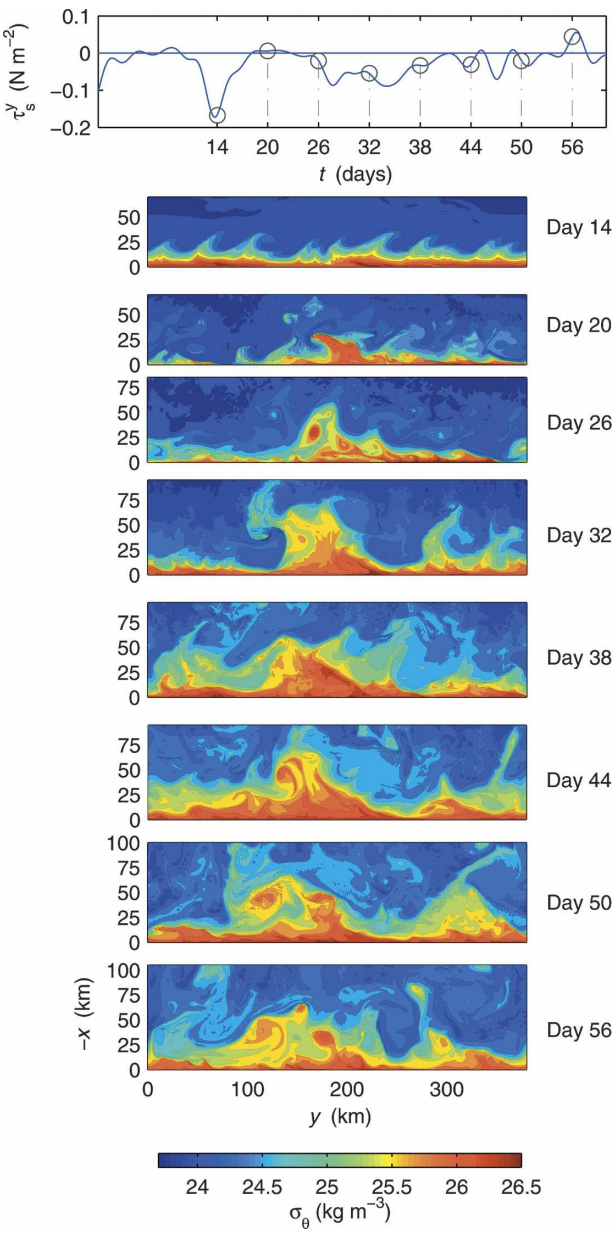

FIG. 20. Fields of surface density (color contours) from days 14 through 56, every 6 days, for the case-3 simulations with realistic Oregon bathymetry. The time variability of the alongshore component of the wind stress is shown on the top.

upwelling front distorts and curls in on itself (day 26), then collapses shoreward (day 38). The spatial variability in the surface density fields from case 3 (Fig. 20) has a noticable qualitative similarity to that in the satellite sea surface temperature plot shown in Fig. 1.

Many of the analyses that were done for the alongshore-uniform channel experiments cannot be repeated for case 3. The variable bathymetry prevents a clear definition of an alongshore-mean and perturbation from that mean. The interaction of effects due to the bathymetry and those due to the instabilities are not seperable as they were in cases 1 and 2 in which the bathymetry presented no alongshore perturbation to the system. Nonetheless the coupling of the two effects is qualitatively apparent. The case-3 simulations contain clearly visible flow–topography interactions as well as features that bear a striking similarity to the instability imposed frontal disturbances examined in the alongshore-uniform simulations.

The enhanced variability that develops on the southern flank of Heceta Bank as a result of the combined effect of the instabilities and bathymetry can be quantified by examining surface fields (upper two panels of Fig. 21) and vertical sections (lower four panels of Fig. 21) of the time-mean density between days 30 and 60, and its standard deviation in the case-3 experiment. As mentioned above, the across-shore deflection of the mean density field generally follows the bathymetric contours. The upwelled water that flows onto the bank from the north (and moves offshore across it) is more dense than the water that upwells on the bank itself, leading to the north–south gradient in time-averaged surface density. The very high standard deviation in surface density in the wake of the bank evidently results from a concentration of disturbance energy related to the high curvature of the mean front in that location. In general, this variability is most intense in the top 75 m of the water column.

6. Summary

Numerical simulations of coastal upwelling using a high-resolution primitive equation model, set up with bathymetry, initial stratification, and forcing representative of Oregon coast summer conditions, reveals the development of frontal instabilities that grow to finite amplitude on a time scale comparable to the rate at which the upwelling flow is evolving. In the periodic channel domain with alongshore-uniform bathymetry and steady winds (case 1) an 8–10 km alongshore scale instability develops at the base of the surface mixed layer approximately 9 days after the onset of the upwelling-favorable winds. Nonlinear effects become of first-order importance in the disturbance evolution within a day. The horizontal structure of the instabilities, as viewed in the surface perturbation density field, distorts such that within 2 days of their initial appearance, successive fluctuations along the front start to interact to produce larger-scale patterns. The surface density field subsequently becomes dominated by irregular disturbances at a 40–80-km scale, which intermittently merge and separate over the last 15 days of the simulation.

The alongshore-uniform bathymetry allows analysis of the exchange of energy between the alongshore-averaged flow and the perturbations. For case 1 with constant wind stress, these analyses show that the primary source of perturbation kinetic energy at the onset of the instability is the potential energy field, indicating that the mechanism for disturbance growth can initially be classified as baroclinic. Potential energy release continues to be the dominant contributor to disturbance growth through approximately the next 7 days of evolution to larger scales. After this point, intermittent increases in the transfer of kinetic energy from the alongshore-averaged flow to the perturbation and concurrent decreases of the potential energy transfer occur. The bursts of kinetic energy transfer tend to be associated with periods of wave–wave interaction in which intermediate-scale irregular disturbances along the front merge to form large-scale features. The kinetic energy transfer from the alongshore-averaged flow diminishes as these large-scale features break apart 2 or 3 days after their formation.

Simulations with temporally variable winds in the alongshore-uniform domain show a similar formation of small alongshore-scale instabilities followed by the development of large-scale disturbances. New instabilities are found to develop on top of the preexisting pattern with each upwelling event. The small-scale instabilities appear to form when isopycnals at the front are warped upward as a result of upwelling-favorable wind events. This, along with the finite-amplitude evolution of the instabilities to larger alongshore scales, suggests that the spatial patterns along upwelling fronts vary as a function of the time since the last upwelling-favorable wind. The across-shore versus time patterns in the perturbation momentum flux divergence and perturbation density flux divergence fields suggest that, despite the onset of new upwelling events, relic disturbance processes associated with earlier upwelling events may persist offshore of the region influenced by the newest disturbances. The time-variable wind simulations also showed that the presence of the instabilities helped sustain across-shore density flux even during periods of relaxed forcing. Relative to the unperturbed 2D simu-

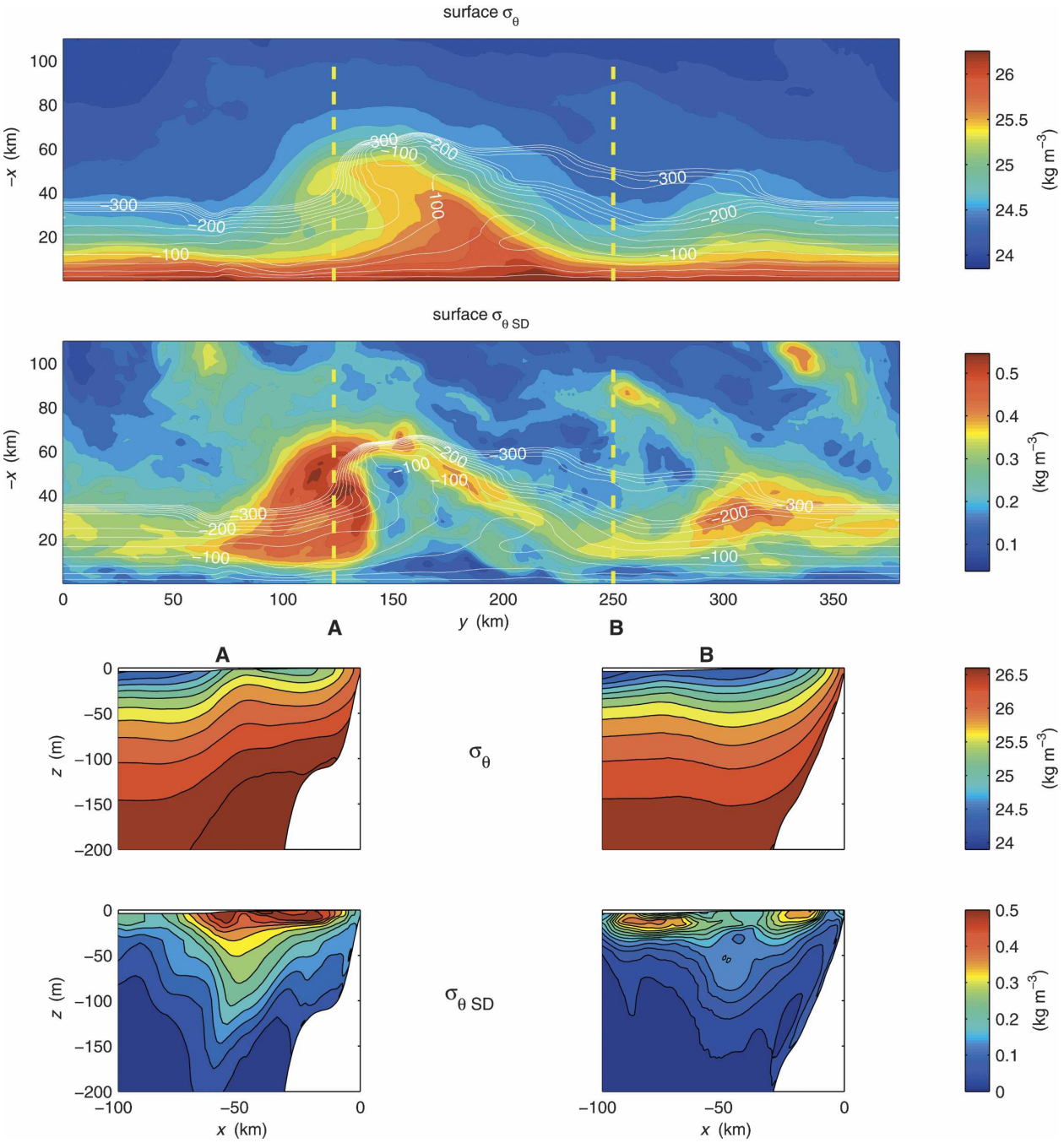

FIG. 21. (top) Surface density field time averaged over days 30–60 for case 3, and (second from the top) the standard deviation of the surface density over the same period. White contour lines in both plots indicate the bathymetry between 50- and 350-m depth, with a contour interval of 25 m. The bottom four panels show corresponding *x*–*z* sections at two transects.

lations, the effect of the instabilities on the time-averaged, alongshore-averaged flow is to produce less steeply sloped isopycnals such that the offshore flow in the surface layer is confined to shallower depths and the alongshore jet is shallower and broader.

Qualitatively similar frontal instabilities develop in a simulation with alongshore-variable bathymetry as well. The instabilities interact with the scales of the upwelling front set by the topographic variations. In the region south of Heceta Bank, the instabilities increase the contortions of the upwelling front resulting in a very complex circulation with greatly enhanced variability in

the surface density field. The combination of the instabilities with bathymetric effects produced patterns in surface density that bear a notable resemblance to those found from satellite images of the surface temperature off the Oregon coast.

Acknowledgments. This research was supported by the Office of Naval Research Ocean Modeling and Prediction Program under Grant N00014-01-1-0285 and by the National Science Foundation under Grants OCE-0218812 and OCE-9907854. The authors are grateful to R. Samelson and J. Barth for helpful comments and suggestions.

REFERENCES

Allen, J. S., P. A. Newberger, and J. Federiuk, 1995: Upwelling circulation on the Oregon continental shelf. Part I: Response to idealized forcing. *J. Phys. Oceanogr.,* **25,** 1843–1866.

Barth, J. A., 1989a: Stability of a coastal upwelling front. Part 1: Model development and stability theorem. *J. Geophys. Res.,* **94,** 10 844–10 856.

——, 1989b: Stability of a coastal upwelling front. Part 2: Model results and comparison with observations. *J. Geophys. Res.,* **94,** 10 857–10 883.

——, 1994: Short-wavelength instabilities on coastal jets and fronts. *J. Geophys. Res.,* **99,** 16 095–16 115.

Charney, J. G., 1947: The dynamics of long waves in a baroclinic westerly current. *J. Meteor.,* **4,** 135–163.

Eady, E. T., 1949: Long waves and cyclone waves. *Tellus,* **1,** 33–52.

Eldevik, T., and K. B. Dysthe, 2002: Spiral eddies. *J. Phys. Oceanogr.,* **32,** 851–869.

Federiuk, J., and J. S. Allen, 1995: Upwelling circulation on the Oregon continental shelf. Part II: Simulations and comparison with observations. *J. Phys. Oceanogr.,* **25,** 1867–1889.

Fukamachi, Y., J. P. McCreary, and J. A. Proehl, 1995: Instability of density fronts in layer and continuously stratified models. *J. Geophys. Res.,* **100,** 2559–2577.

Klaassen, G. P., and W. R. Peltier, 1989: The role of transverse secondary instabilities in the evolution of free shear layers. *J. Fluid Mech.,* **202,** 367–402.

Large, W. G., J. C. McWilliams, and S. C. Doney, 1994: Oceanic vertical mixing: A review and a model with a nonlocal boundary layer parameterization. *Rev. Geophys.,* **32,** 363–403.

McCreary, J. P., Y. Fukamachi, and P. K. Kundu, 1991: A numerical investigation of jets and eddies near an eastern ocean boundary. *J. Geophys. Res.,* **96,** 2515–2534.

Mellor, G. L., and T. Yamada, 1982: Development of a turbulence closure model for geophysical fluid problems. *Rev. Geophys.,* **20,** 851–875.

Oke, P. R., J. S. Allen, R. N. Miller, and G. D. Egbert, 2002a: A modeling study of the three-dimensional continental shelf circulation off Oregon. Part II: Dynamical analysis. *J. Phys. Oceanogr.,* **32,** 1383–1403.

——, ——, ——, ——, J. A. Austin, J. A. Barth, J. Boyd, and P. M. Kosro, 2002b: A modeling study of the three-dimensional continental shelf circulation off Oregon. Part I: Model–data comparisons. *J. Phys. Oceanogr.,* **32,** 1360–1382.

Orlanski, I., and M. D. Cox, 1973: Baroclinic instability in ocean currents. *Geophys. Fluid Dyn.,* **4,** 297–332.

Pedlosky, J., 1987: *Geophysical Fluid Dynamics.* 2d ed. Springer-Verlag, 710 pp.

Shchepetkin, A. F., and J. McWilliams, 1998: Quasi-monotone advections schemes based on explicit locally adaptive dissipation. *Mon. Wea. Rev.,* **126,** 1541–1580.

——, and ——, 2005: The Regional Ocean Modeling System (ROMS): A split-explicit free-surface topography-following coordinates ocean model. *Ocean Modell.,* **9,** doi:10.1016/j.ocemod.2004.08.002.

Shi, X. B., and L. P. Roed, 1999: Frontal instabilities in a two-layer, primitive equation ocean model. *J. Phys. Oceanogr.,* **29,** 948–968.

Yamazaki, Y. H., and W. R. Peltier, 2001: The existence of subsynoptic baroclinic instability and the nonlinear evolution of shallow disturbances. *J. Atmos. Sci.,* **58,** 657–683.